Science Advances
AAAS

Supplementary Materials for

On-surface synthesis of Heisenberg spin-1/2 antiferromagnetic molecular chains

Kewei Sun *et al.*

Corresponding author: Shigeki Kawai, kawai.Shigeki@nims.go.jp; Adam S. Foster, adam.foster@aalto.fi; Shingo Ito, sgito@ntu.edu.sg

Sci. Adv. **11**, eads1641 (2025)
DOI: 10.1126/sciadv.ads1641

This PDF file includes:

Supplementary Materials

Synthesis of 1

General: All reactions were carried out under argon or nitrogen atmosphere using standard Schlenk techniques, unless otherwise noted. Thin-layer chromatography was performed using glass plates pre-coated with silica gel impregnated with a fluorescent indicator (Merck, #1.05715.0001). Silica gel column chromatography was performed as described by Still, et al. (*53*), employing silica gel 60N (spherical, neutral) purchased from W. R. Grace, Ltd.

Instrumentation: NMR spectra were recorded on Bruker Avance 400 and Bruker Avance III 400 spectrometers. Chemical shift values for protons are referenced to the signal of tetramethylsilane (δ = 0.00) or the residual signal of dimethyl sulfoxide-*d6* (δ = 2.50), and chemical shift values for carbons are referenced to the signal of tetramethylsilane (δ = 0.00) or the carbon resonance of chloroform-*d* (δ = 77.2) and dimethyl sulfoxide-*d6* (δ = 39.5). Infrared (IR) spectra were recorded on a PerkinElmer FTIR spectrum 100 with an attenuated total reflection (ATR) sampling accessary. High-resolution mass (HRMS) spectra were taken on a Waters Q-Tof Premier mass spectrometer with an electron spray ionization time-of-flight (ESI-TOF) method. Decomposition points and melting points were recorded on an OptiMelt MPA-100 apparatus.

Materials: The following reagents were purchased from indicated suppliers and used as received: benzo[*c*][1,2]oxaborol-1(3*H*)-ol (**II**; Fluorochem Ltd.), potassium carbonate (K_2CO_3, Tokyo Chemical Industry, Co. Ltd. (TCI)), tetrakis(triphenylphosphine)palladium(0) (Pd(PPh3)4; Sigma-Aldrich), tributylamine (Bu_3N, TCI), dimethylsulfoxide (DMSO; TCI). 4-Chloro-2,6-diiodoaniline was prepared according to a literature procedure (*54*).

Synthesis of Compound III

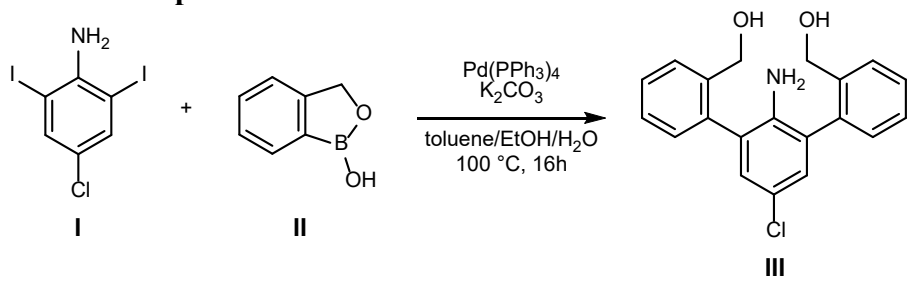

I **II** **III**

In a 25 mL Schlenk tube, 4-chloro-2,6-diiodoaniline (**I**, 0.20 g, 0.70 mmol), benzo[*c*][1,2]oxaborol-1(3*H*)-ol (**II**, 0.24 g, 1.75 mmol), tetrakis(triphenylphosphine)palladium(0) ($Pd(PPh_3)_4$, 41 mg, 0.035 mmol), and potassium carbonate (K_2CO_3, 0.78 g, 5.6 mmol) were dissolved in toluene (5.0 mL), ethanol (1.0 mL), and water (1.0 mL). After being stirred for 16 h at 100 °C, the mixture was allowed to cool down to room temperature, and extracted with ethyl acetate. The combined organic phase was washed with water, dried under sodium sulfate (Na_2SO_4), filtered, and evaporated to dryness. The crude product was purified by column chromatography (Hex: EA = 4:1 to 1:2) to afford compound **III** as a colorless solid (200 mg, 0.59 mmol, 84%).

Colorless solid; R_f = 0.26 (hexane/ethyl acetate = 1/1); mp 193–195 °C; IR (neat) cm^{-1} 3384, 3269, 1615, 1489, 1454, 1429, 1197, 1114, 1035, 1007, 950, 873, 764, 740, 710; In NMR spectra, two rotational isomers were observed in the ratio of *ca.* 6:4, ^{1}H NMR (400 MHz, DMSO-d_6) *major*

isomer: δ 7.63 (d, *J* = 7.5 Hz, 2H), 7.43 (t, *J* = 7.6 Hz, 2H), 7.35 (t, *J* = 7.0 Hz, 2H), 7.22–7.13 (m, 2H), 6.97 (s, 2H), 5.12 (t, *J* = 5.5 Hz, 2H), 4.45–4.28 (m, 4H), 3.76 (s, 2H), *minor* isomer: δ 7.62 (d, *J* = 7.2 Hz, 2H), 7.43 (t, *J* = 7.6 Hz, 2H), 7.36 (t, *J* = 7.4 Hz, 2H), 7.22–7.13 (m, 2H), 6.97 (s, 2H), 5.08 (t, *J* = 5.4 Hz, 2H), 4.45–4.28 (m, 4H), 3.77 (s, 2H); ^{13}C NMR (101 MHz, DMSO-d_6) *major* isomer: δ 141.4, 141.3, 135.8, 130.0, 128.9, 128.5, 127.9, 127.6, 127.5, 120.3, 60.7. *minor* isomer: δ 141.4, 141.0, 136.0, 130.1, 128.9, 128.5, 127.9, 127.7, 127.6, 120.2, 60.9; HRMS (ESI) *m*/*z* calcd for $C_{20}H_{18}ClNO_2$ $[M+H]^+$ 340.1104, found 340.1115.

Synthesis of Compound IV

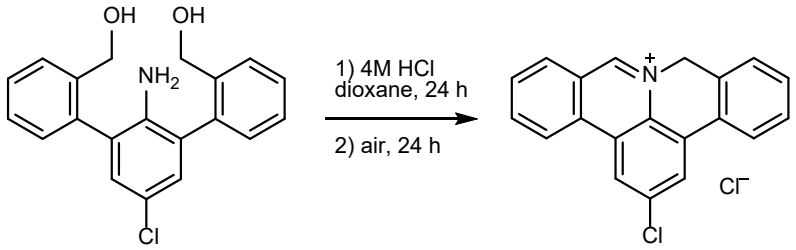

III **IV**

In a 50 mL Schlenk tube, compound **III** (200 mg, 0.59 mmol) was dissolved in 4M HCl in dioxane (12 mL, 48 mmol) under inert atmosphere. The mixture was stirred for 24 h at 120 ° C. After cooling down to room temperature, the cap of the Schlenk tube was removed. The mixture was stirred under air for 24 h at room temperature. The resulting precipitate was collected by filtration and washed with diethyl ether to afford compound **IV** as a yellow solid (186 mg, 0.55 mmol, 93%).

Yellow solid; mp 225–227 (dec.); IR (neat) cm^{-1} 3066, 1622, 1596, 1579, 1531, 1504, 1423, 1392, 1348, 1244, 1230, 1133, 1119, 1047, 903, 872, 839, 786, 756, 728, 708; ^{1}H NMR (400 MHz, DMSO-d_6) δ 10.38 (s, 1H), 9.18 (s, 1H), 9.17 (d, *J* = 5.9 Hz, 1H), 8.80 (d, *J* = 1.6 Hz, 1H), 8.66 (t, *J* = 7.7 Hz, 1H), 8.44–8.33 (m, 2H), 8.15 (t, *J* = 7.5 Hz, 1H), 7.64–7.55 (m, 3H), 6.28 (s, 2H); ^{13}C NMR (101 MHz, DMSO-d_6) δ 155.0, 138.6, 136.8, 133.6, 133.1, 131.7, 131.1, 129.8, 129.1, 129.1, 129.0, 128.1, 126.9, 126.4, 125.9, 125.1, 124.7, 124.4, 123.8, 57.5; HRMS (ESI) *m*/*z* calcd for $C_{20}H_{13}ClN$ $[M]^+$ 302.0737, found 302.0739.

Synthesis of Compound 1

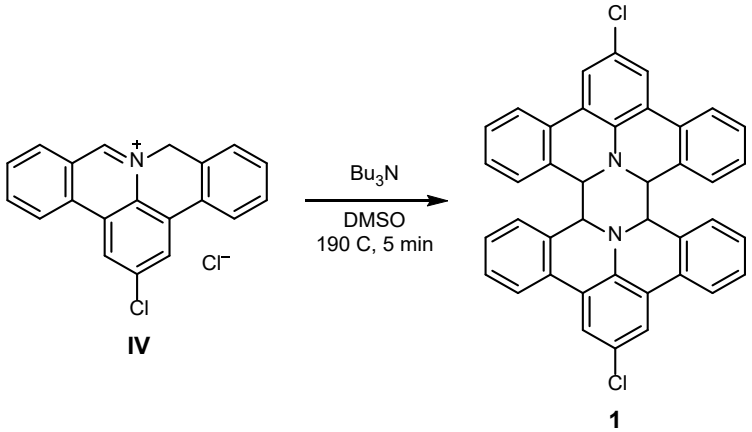

IV **1**

A solution of compound **IV** (10 mg, 0.030 mmol) dissolved in dimethylsulfoxidea (DMSO; 2.0 mL) was preheated to 190 °C for 30 seconds. Subsequently, tributylamine (0.17 mL, 0.71 mmol) was added and further stirred for 5 min. After cooling down to room temperature, the reaction

mixture was extracted with dichloromethane. The combined organic phases were washed with water, dried under sodium sulfate (Na_2SO_4), filtered, and evaporated *in vacuo*. The crude product was purified by silica gel column chromatography (hexane/dichloromethane = 8/1) to afford compound **1** as a yellow solid (1.3 mg, 0.002 mmol, 7%).

Yellow solid; R_f = 0.30 (hexane/dichloromethane = 4/1); mp >300 °C; IR (neat) cm^{-1} 2921, 2852, 1708, 1577, 1496, 1481, 1432, 1388, 1327, 1297, 1229, 1160, 1104, 1049, 941, 841, 778, 752, 730, 686; ^1H NMR (400 MHz, $CDCl_3$) δ 7.71 (s, 4H), 7.59 (d, J = 8.0 Hz, 4H), 7.26 (t, J = 8.0 Hz, 4H), 6.86 (t, J = 8.0 Hz, 4H), 6.02 (d, J = 8.0 Hz, 4H), 5.11 (s, 4H); ^{13}C NMR (101 MHz, $CDCl_3$) δ 139.1 (2C), 129.7 (4C), 129.09 (4C), 128.8 (4C), 128.5 (4C), 127.3 (4C), 124.5 (2C), 124.2 (4C), 123.1 (4C), 122.0 (4C), 61.5 (4C); HRMS (ESI) m/z calcd for $C_{40}H_{24}Cl_2N_2$ $[M+H]^+$ 603.1395, found 603.1399.

Supplementary Note 1
DFT simulations of STM and d*I*/d*V* maps:
Fig. S6A,B show two experimental d*I*/d*V* maps of the N_2HBC^+ molecule acquired at zero bias. The simulations in fig. S6C calculated with a flexible CO tip show that the features of fig. S6A are correctly captured by the simulations at near tip-sample distance, especially at the brighter inner part of the molecule. In this scenario, the flexibility of the CO tip is important to enhance the contrast of the image. As the tip-sample distance increases, the flexibility of the CO tip becomes less important, and the simulations start to resemble more the experimental image in fig. S6B. Fig. S7 shows a series of d*I*/d*V* maps acquired with a rigid CO tip, resembling even more the experimental image in fig. S6B. Fig. S7 also shows simulated d*I*/d*V* maps calculated with different tip conditions, where we found that a linear combination of 5% of *s* and 95% of p_{xy} of the tip orbitals best resembles the experimental images.

Supplementary Note 2
Mean-field Hubbard *vs.* spin-polarized DFT calculations of periodic chains:
We investigated the electronic and magnetic properties of the periodic N_2HBC^+ chains by using mean-field Hubbard model and spin-polarized DFT, which have been widely used to determine the magnetization of nanographenes and demonstrate agreement with experiments (*3*). Both mean-field Hubbard and spin-polarized DFT calculations predict the antiferromagnetic alignment to be energetically favored (details can be found in the main text). The presence of a nitrogen is included in the tight binding model as a site with a local negative onsite energy, and its different charge state is accounted for in the filling of the system. We performed self-consistent calculations of the tight binding model, allowing access to the self-consistent magnetization, charge density and electronic structure (*48*). In the absence of spin polarization, the periodic chains display metallic band structures, as shown in fig. S14A,B and S15B. Spin polarization results in an increased bandgap and the localization of electronic states at the center of each unit with an antiferromagnetic ordering, as shown in the calculated spin density maps (fig. S14C,D and S15A,C). The calculated spin density distributions align with the experimentally resolved spin localization at the center of each unit of the chains (Fig. 4 of the main text). In our calculation, we use only the nearest neighbors hopping. The hopping term *t* is set to a constant value of 2.7 eV. As shown in fig. S14E, the mean-field Hubbard model calculations show that the exchange interaction *J* for periodic chains varies substantially as a function of the on-site Coulomb repulsion *U*. This variation suggests the sensitive dependence of the exchange interaction on the on-site electronic interaction characterized by *U*. We find that exchange couplings compatible with the DFT calculations and our experimental observation are obtained for a value of $U = 1.5\ t$, similar to other nanographene systems.

Supplementary Note 3
DFT calculations of the antiferromagnetic chains:
PBE/DFT-calculated work functions of neutral and positively charged chains (Table S1) shows that charge transfer is always necessary to allow the Fermi level alignment of the chains with gold in relation to the vacuum. For the N_2HBC molecule, dimer- and trimer-N_2HBC, our calculations clearly indicate that all systems will be positively charged due to a local transfer of approximately one electron to gold from each N_2HBC unit. For larger chains such as tetramer and pentamer, charging the whole system in the calculation led to unphysical results. Specifically, when the pentamer was modeled with +5 charges (one electron donated per N_2HBC unit), the resulting

electronic structure shows delocalized effects that are inconsistent with the local charge transfer between the system and substrate (fig. S13). These unphysical results arise from the limitations of DFT when simulating large, multi-charged systems. To avoid this delocalization effect, we used a periodic model in our simulations. The simulations correctly capture the electronic structure of the inner N_2HBC units, while the end states in the finite system are not properly resolved (as shown in Fig. 3). Despite this limitation, our simulations accurately reflect the core electronic structure of the pentamer. Based on these results, we conclude that each N_2HBC unit donates approximately one electron to the Au(111) substrate regardless of the size of the chain. We also propose that the same behavior will be observed for even longer chains, approaching the infinite-chain regime.

Regarding the geometrical structure of the N_2HBC molecule and chains, we noticed that they are strongly distorted if fully relaxed (fig. S19), indicating that, besides the charge transfer, the Au(111) substrate is necessary for structural stability of the chains. Thus, all the free-standing calculations were realized allowing relaxation only in the x-y plane.

After geometry relaxation, the energy levels and molecular orbitals shown in fig. S20 and S21 were obtained within the B3LYP level. In fig. S20A, the SOMO-SUMO gap of the N_2HBC^+ molecule is 1.26 eV, and both SOMO and SUMO in fig. S20B have the same spatial distributions. The SOMO-SUMO gap of the open shell singlet dimer-N_2HBC^{2+} in fig. S20C is 1.22 eV, and the SOMO and SUMO have opposite spatial distributions depending on the spin (fig. S20D). On the other hand, fig. S20E shows that the SOMO-SUMO gap of the triplet dimer-N_2HBC^{2+} is much smaller (0.99 eV), which also changes completely the spatial distribution of the orbitals (fig. S20F). The triplet dimer-N_2HBC^{2+} is 27 meV higher in energy than its open-shell singlet ground state, which is comparable to the experimental value of the super exchange coupling shown in fig. S16. The energy levels and molecular orbitals of the trimer-N_2HBC^{3+} are shown in fig. S21. The low-energy molecular orbitals of the trimer-N_2HBC^{3+} in the $S = 1/2$ and $S = 3/2$ states are either spatially very localized at its central N_2HBC^+ unit or at its peripheral units. The $S = 3/2$ trimer-N_2HBC^{3+} is 62 meV higher in energy than its $S = 1/2$ ground state.

Supplementary Note 4

Analytical solution for three interacting spin ½ electrons in a linear chain

The Heisenberg Hamiltonian of such system can be written as:

$$\widehat{H} = J\left(\overrightarrow{S_1} \cdot \overrightarrow{S_2}\right) + J\left(\overrightarrow{S_2} \cdot \overrightarrow{S_3}\right)$$

which can be expressed in terms of the spin-ladder operators $S_n^{\pm} = S_n^x \pm iS_n^y$:

$$\overrightarrow{S_1} \cdot \overrightarrow{S_2} = S_1^x S_2^x + S_1^y S_2^y + S_1^z S_2^z = \frac{1}{2}(S_1^+ S_2^- + S_1^- S_2^+) + S_1^z S_2^z.$$

For three spins, the total spin S_T can take values of a doublet $\pm 1/2$ and quartet $\pm 3/2$. The 2^3 possible states for the three spin 1/2 system are:

$$|\uparrow\uparrow\uparrow\rangle, |\uparrow\uparrow\downarrow\rangle, |\uparrow\downarrow\uparrow\rangle, |\uparrow\downarrow\downarrow\rangle, |\downarrow\uparrow\uparrow\rangle, |\downarrow\uparrow\downarrow\rangle, |\downarrow\downarrow\uparrow\rangle, |\downarrow\downarrow\downarrow\rangle.$$

Hence, taking *J* as a common factor, the Hamiltonian matrix takes the following form in this basis:

	$\|\uparrow\uparrow\uparrow\rangle$	$\|\uparrow\uparrow\downarrow\rangle$	$\|\uparrow\downarrow\uparrow\rangle$	$\|\uparrow\downarrow\downarrow\rangle$	$\|\downarrow\uparrow\uparrow\rangle$	$\|\downarrow\uparrow\downarrow\rangle$	$\|\downarrow\downarrow\uparrow\rangle$	$\|\downarrow\downarrow\downarrow\rangle$
$\langle\uparrow\uparrow\uparrow\|$	½	0	0	0	0	0	0	0
$\langle\uparrow\uparrow\downarrow\|$	0	0	½	0	0	0	0	0
$\langle\uparrow\downarrow\uparrow\|$	0	½	-½	0	½	0	0	0
$\langle\uparrow\downarrow\downarrow\|$	0	0	0	0	0	½	0	0
$\langle\downarrow\uparrow\uparrow\|$	0	0	½	0	0	0	0	0
$\langle\downarrow\uparrow\downarrow\|$	0	0	0	½	0	-½	½	0
$\langle\downarrow\downarrow\uparrow\|$	0	0	0	0	0	½	0	0
$\langle\downarrow\downarrow\downarrow\|$	0	0	0	0	0	0	0	½

The two many-body doublet ground states can be written as:

$$|\alpha\rangle = \frac{1}{\sqrt{6}}(|\uparrow\uparrow\downarrow\rangle - 2|\uparrow\downarrow\uparrow\rangle + |\downarrow\uparrow\uparrow\rangle) \text{ and } |\beta\rangle = \frac{1}{\sqrt{6}}(|\uparrow\downarrow\downarrow\rangle - 2|\downarrow\uparrow\downarrow\rangle + |\uparrow\downarrow\downarrow\rangle),$$

which are the states that contribute to the spin correlator at zero bias. The other excited many-body states are:

$$|\varphi_1\rangle = \frac{1}{\sqrt{2}}(|\uparrow\uparrow\downarrow\rangle - |\downarrow\uparrow\uparrow\rangle); \qquad |\varphi_2\rangle = \frac{1}{\sqrt{2}}(|\uparrow\downarrow\downarrow\rangle - |\uparrow\downarrow\downarrow\rangle);$$

$$|\varphi_3\rangle = \frac{1}{\sqrt{3}}(|\uparrow\uparrow\downarrow\rangle + |\uparrow\downarrow\uparrow\rangle + |\downarrow\uparrow\uparrow\rangle); \qquad |\varphi_4\rangle = \frac{1}{\sqrt{3}}(|\uparrow\downarrow\downarrow\rangle + |\downarrow\uparrow\downarrow\rangle + |\downarrow\downarrow\uparrow\rangle);$$

$$|\varphi_5\rangle = |\uparrow\uparrow\uparrow\rangle; \qquad |\varphi_6\rangle = |\downarrow\downarrow\downarrow\rangle$$

Supplementary Note 5

Magnetic properties of N_2HBC chains on a $AuSi_X$ layer formed on Au(111)

To verify the robustness of magnetic properties of the N_2HBC chains, we formed a $AuSi_X$ intercalation layer between the nanostructures and the Au(111) substrate by depositing Si atoms on the sample (*21*,*43*,*44*). The STM topography shows N_2HBC chains and GNR 4 oligomers on the $AuSi_X$/Au(111) surface (fig. S24A). A close-up image exhibits individual monomer **3**, in which the morphology is approximately symmetrical (inset of fig. S24B). A Kondo resonance zero-bias peak is detected in the d*I*/d*V* spectrum (fig. S24B) recorded over the N_2HBC molecule, demonstrating a stronger intensity at the molecular center, as shown in the d*I*/d*V* map at 0 mV (fig. S24C). In contrast, an individual dimer-N_2HBC, reveals a slight asymmetric signal probably due to the underlying heterogeneous $AuSi_X$ area (inset of fig. S24D). d*I*/d*V* curves (fig. S24D) recorded over the dimer-N_2HBC exhibit unprecedented spin excitation spectra, in which two sharp peaks at ±43 mV are unambiguously identified. Spatial distribution of spin excitation states is shown in

d*I*/d*V* maps at ±43 mV in fig. S24E,F, revealing approximately symmetrical patterns. Trimer-N_2HBC (inset of fig. S24G) is also slightly asymmetrical as the case of dimer-N_2HBC. d*I*/d*V* curves (fig. S24G) recorded over the trimer-N_2HBC show the zero-bias peaks at the unit on both sides, yet step-like features at the central unit, which is similar to observations on Au(111). fig. S24H,I exhibit the d*I*/d*V* maps at 0 mV and 40 mV over the-trimer-N_2HBC, revealing the spatial distribution of the Kondo resonance state and spin excitation state.

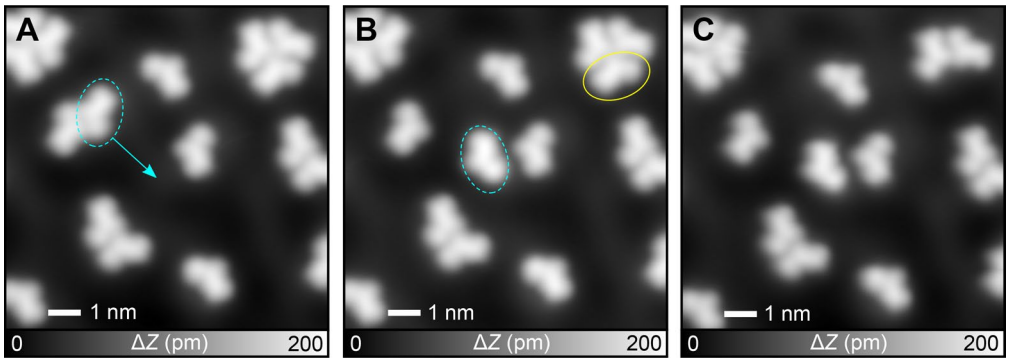

Fig. S1. **A series of tip-induced manipulations of molecules 2.** (**A**) STM topography of as-deposited **1** on Au(111). The blue ellipse and arrow indicate the target molecule **2** and the trajectory of tip movement. (**B**) STM topography taken after tip-induced manipulation. The blue ellipse indicates the manipulated molecule **2**. The yellow ellipse indicates the tip approaching another **2**. (**C**) STM topography taken after the molecule **2** adsorbed onto the tip apex. Measurement parameters: $V = 50$ mV and $I = 10$ pA.

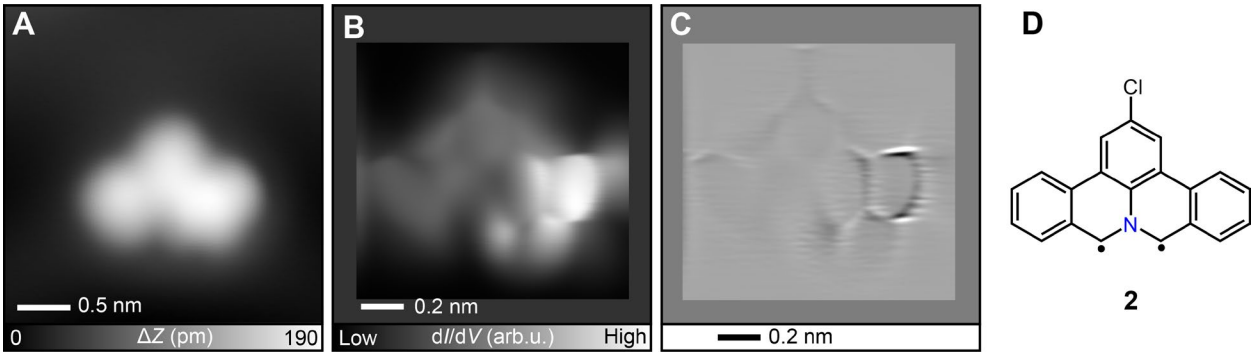

Fig. S2. **STM characterization of 2.** (**A**) STM topography of an individual **2** on Au(111). (**B-D**) Constant height dI/dV map (B), the corresponding Laplace filtered image (C), and Chemical structure of **2** (D). Measurement parameters: $V = 50$ mV and $I = 5$ pA.

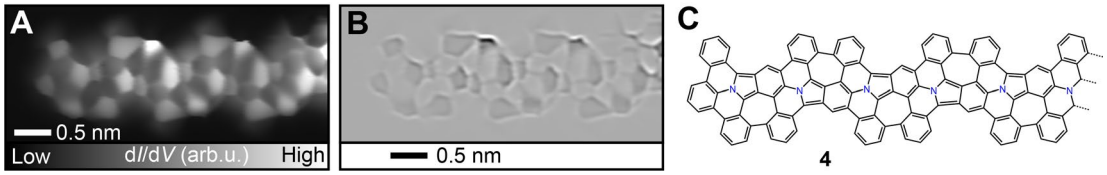

Fig. S3. **STM characterization of 4.** (**A**) Bond-resolved STM image of individual **4** on Au(111). (**B**) The corresponding Laplace filtered image and (**C**) the chemical structure. Measurement parameters: $V = 1$ mV and $V_{ac} = 10$ mV in (A).

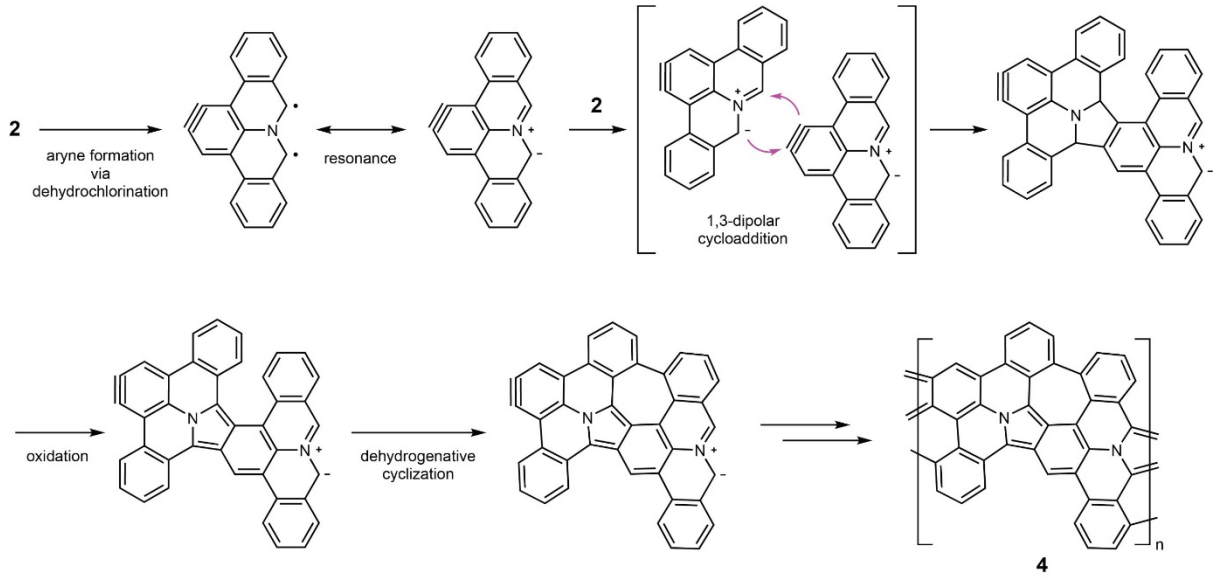

Fig. S4. Reaction path to synthesize **4**.

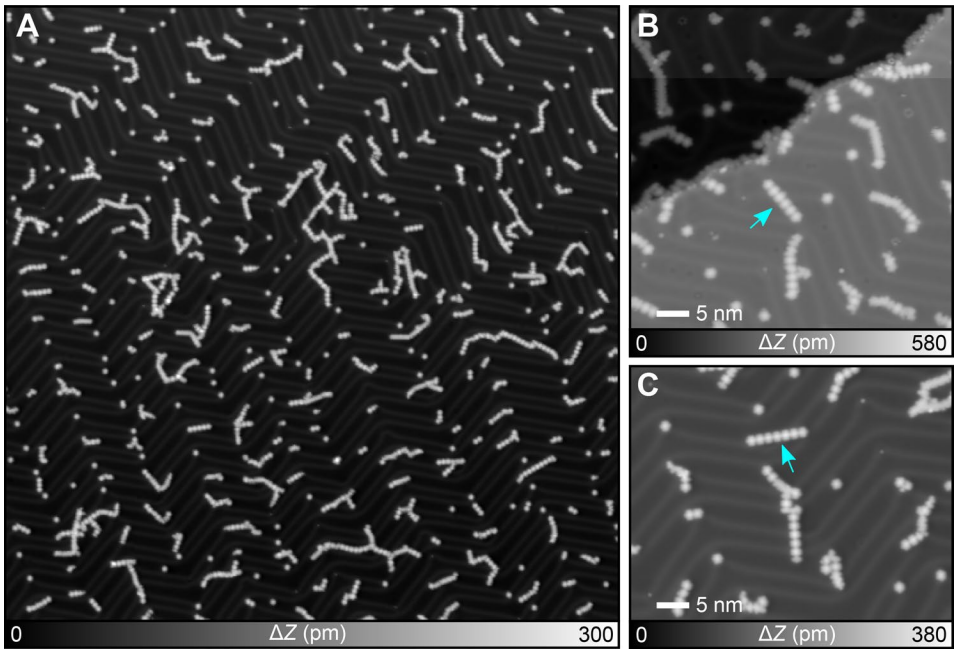

Fig. S5. On-Surface synthesis of N_2HBC oligomers. (**A**) Large-scale STM topography of the Au(111) surface following the growth of N_2HBC oligomers. (**B**,**C**) Close-up STM images. The hexamer and heptamer of N_2HBC are distinctly visible. Measurement parameters: V = 200 mV and I = 5 pA.

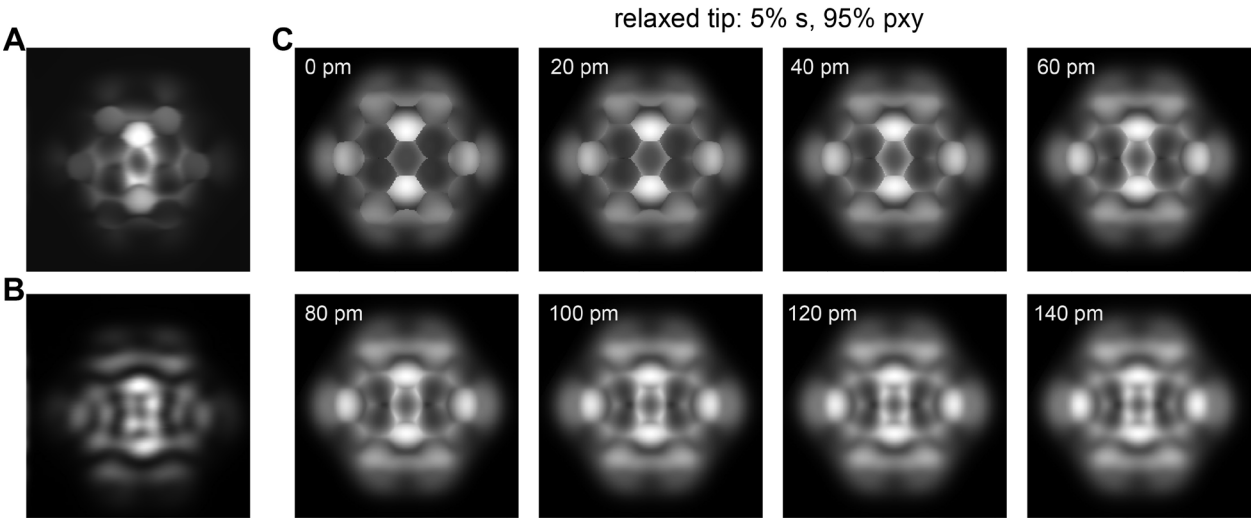

Fig. S6. Experimental and simulated d*I*/d*V* maps of individual N_2HBC. (**A**,**B**) Two different experimental d*I*/d*V* maps acquired at zero bias voltage at different tip-sample distances. (**C**) Constant height d*I*/d*V* simulations were realized considering a flexible CO tip.

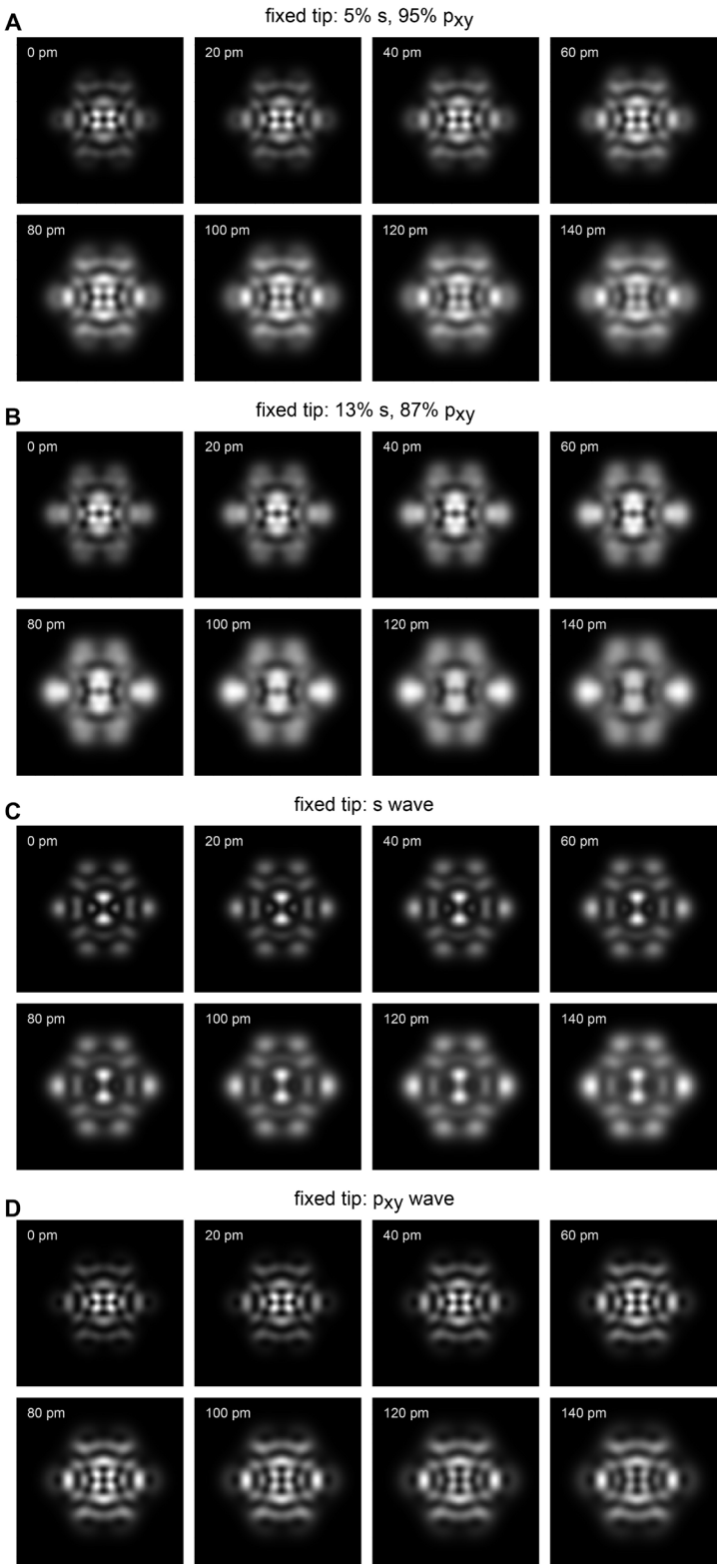

Fig. S7. Simulated d*I*/d*V* maps of individual N_2HBC. A series of constant height d*I*/d*V* simulations obtained with mixed *s* and p_{xy}-wave tips, which were acquired through a linear combination of *s* and p_{xy} orbitals with different weights. The mixing was realized to simulate the effect of a rigid CO tip attached to the tip apex.

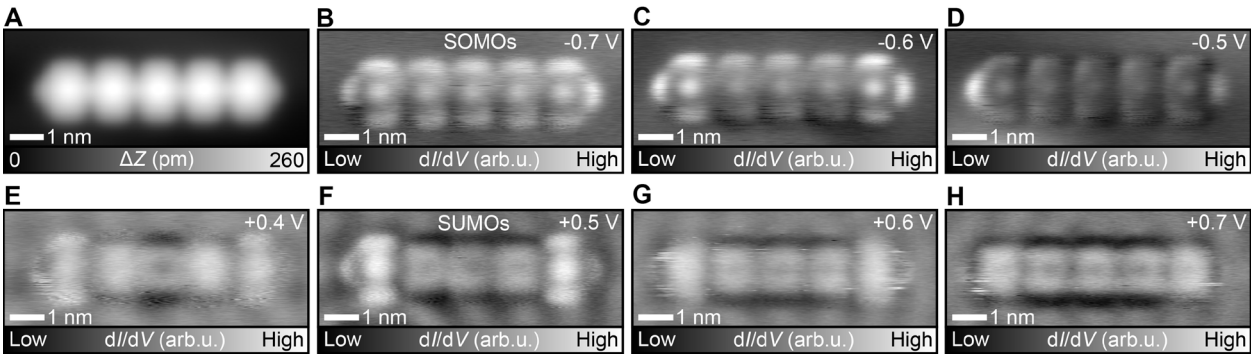

Fig. S8. Electronic properties of an individual pentamer of N_2HBC. (**A**) STM topography. (**B-H**) Constant current dI/dV maps measured at different bias voltages around the energy of SUMOs and SUMOs. Measurement parameters: V = 200 mV and I = 10 pA in (A). For STS measurement, the tip-sample distance was adjusted at the corresponding bias voltages and I = 160 pA, V_{ac} = 10 mV in (B-D) (F-H). I = 150 pA, V_{ac} = 10 mV in (E).

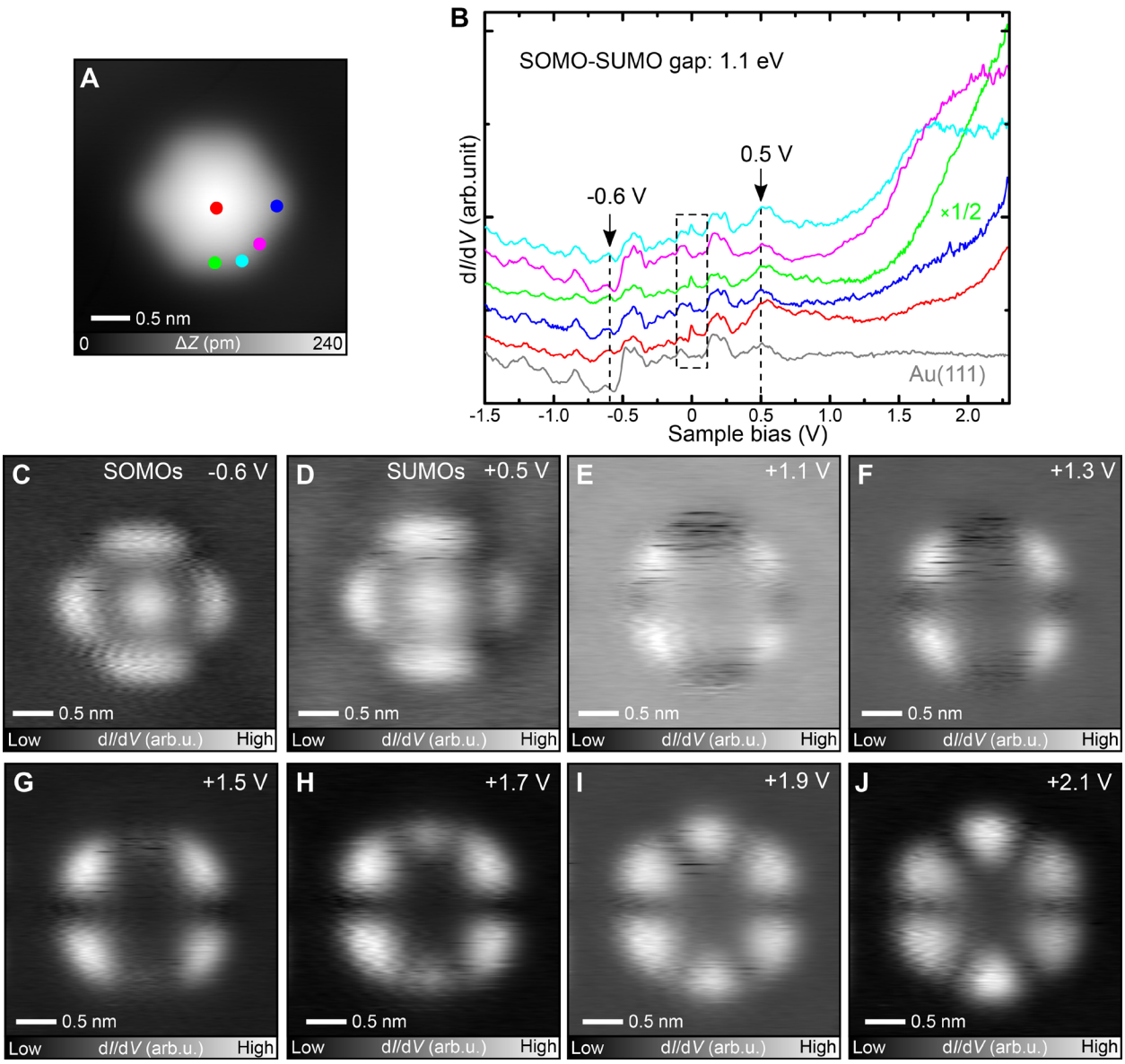

Fig. S9. Electronic properties of an individual N_2HBC. (**A**) STM topography. (**B**) dI/dV curves recorded at different sites as indicated by colored dots in (A). (**C-J**) Constant current dI/dV maps measured at different bias voltages. Measurement parameters: V = 200 mV and I = 10 pA on (A).

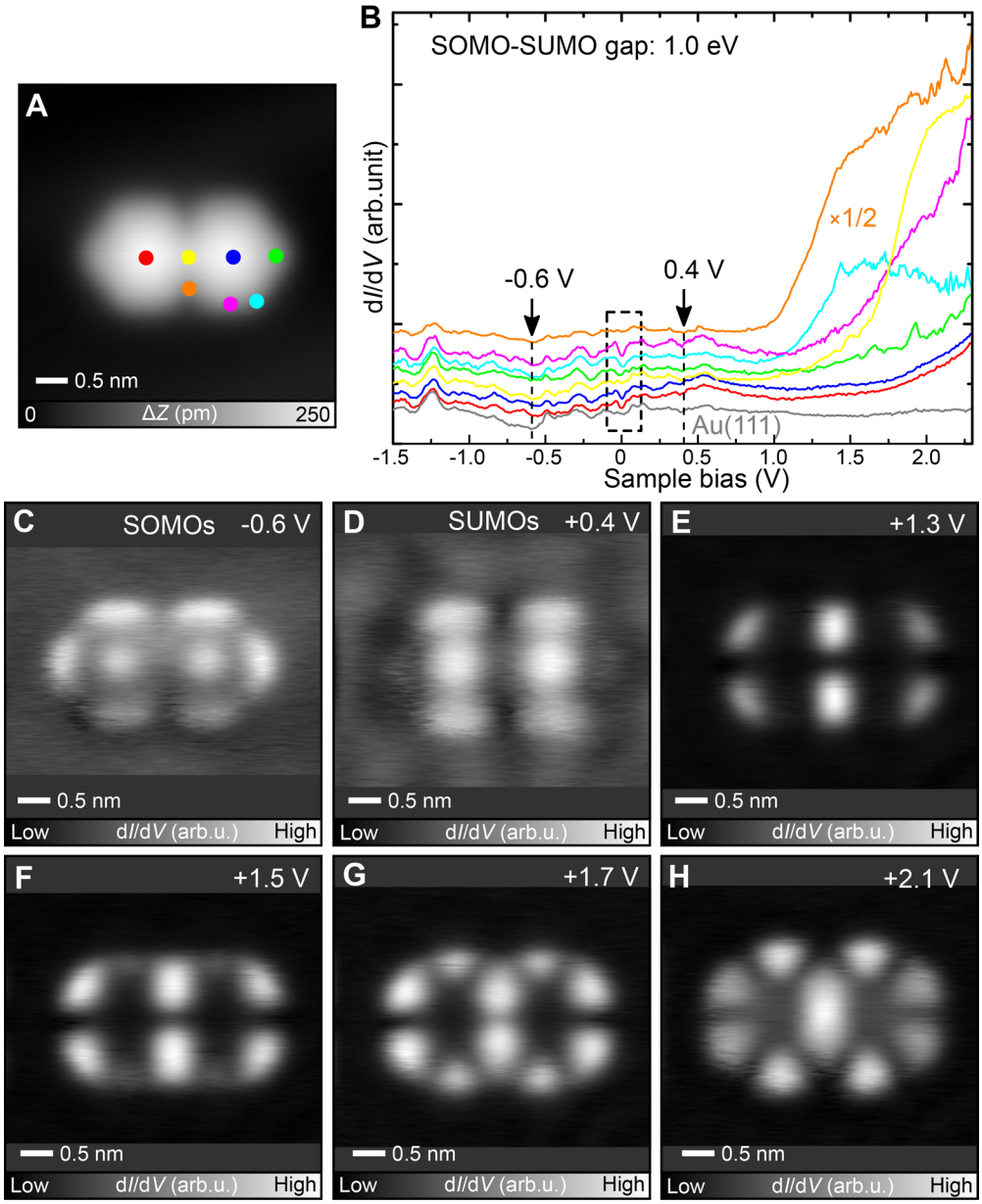

Fig. S10. Electronic properties of a dimer of N_2HBC. (**A**) STM topography. (**B**) dI/dV curves recorded at different sites as indicated by colored dots in (A). (**C-H**) Constant current dI/dV maps measured at different bias voltages. Measurement parameters: V = 200 mV and I = 10 pA in (A).

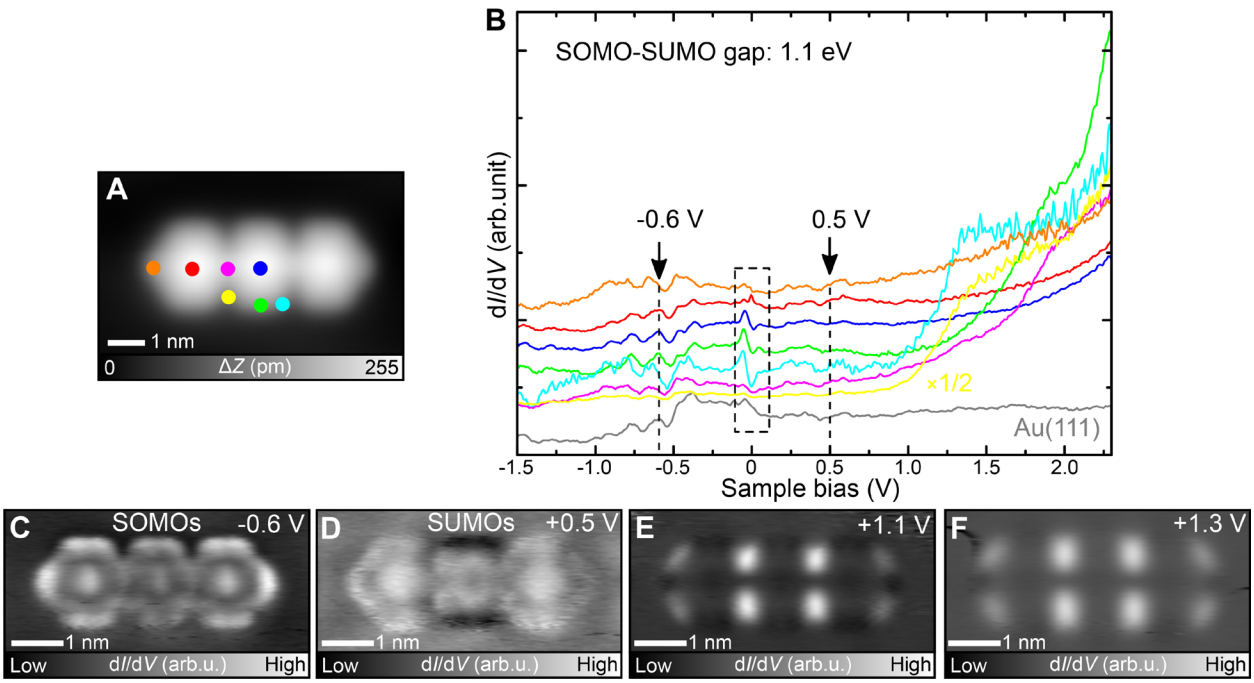

Fig. S11. Electronic properties of a trimer of N_2HBC. (**A**) STM topography. (**B**) dI/dV curves recorded at different sites as indicated by colored dots in (A). (**C-F**) Constant current dI/dV maps measured at different bias voltages. Measurement parameters: V = 200 mV and I = 10 pA in (A).

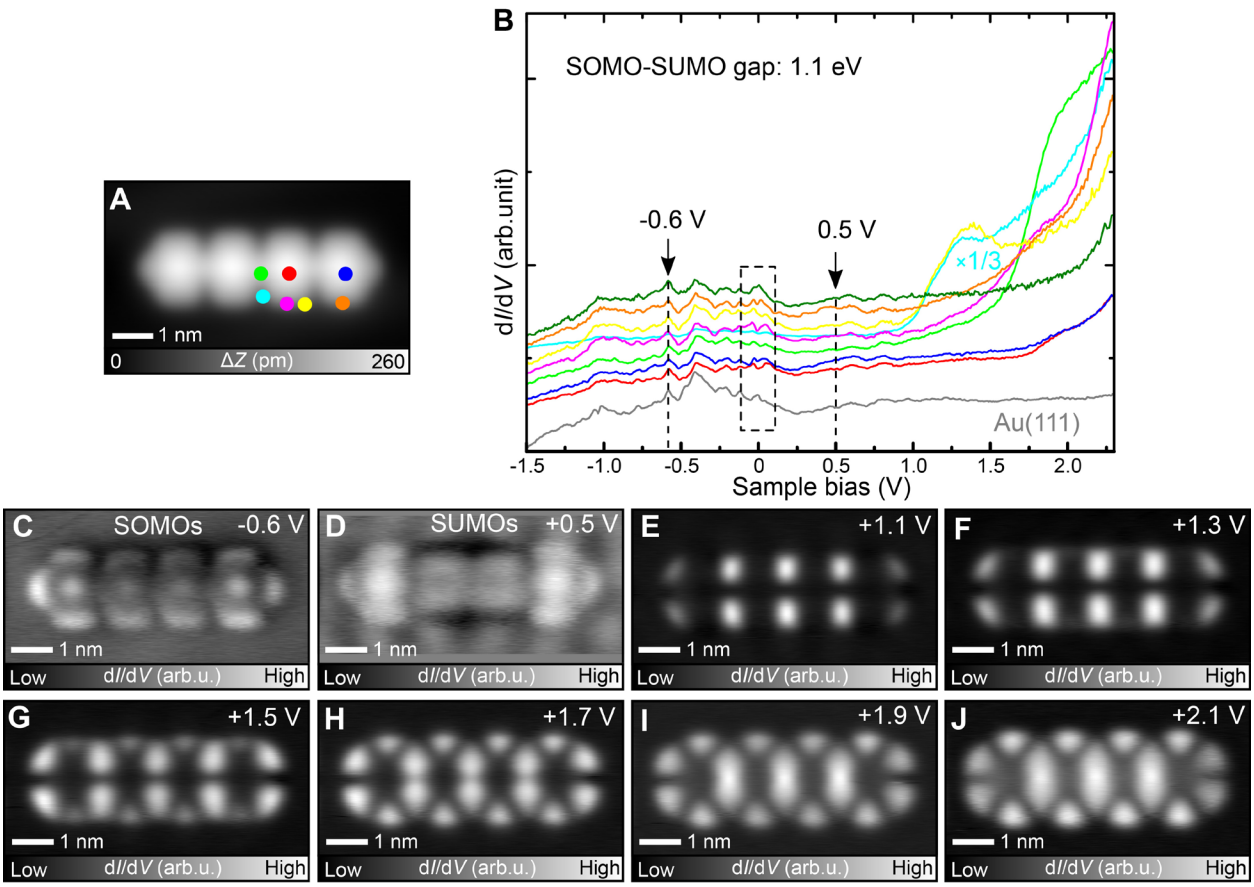

Fig. S12. Electronic properties of a tetramer of N_2HBC. (**A**) STM topography. (**B**) dI/dV curves recorded at different sites as indicated by colored dots in (A). (**C-J**) Constant current dI/dV maps measured at different bias voltages. Measurement parameters: V = 200 mV and I = 10 pA in (A).

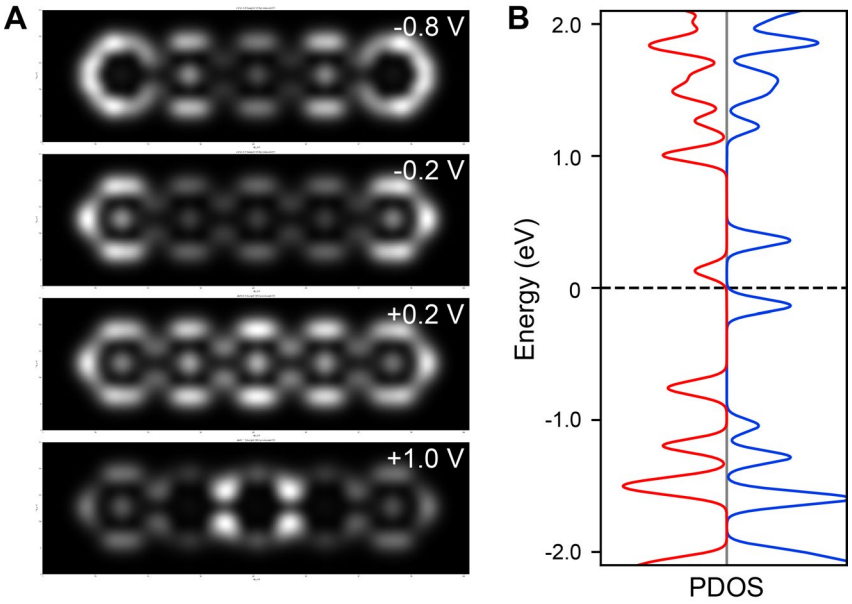

Fig. S13. DFT simulations of electronic properties of an individual pentamer of N_2HBC at B3LYP level. (**A**) Constant height d*I*/d*V* maps calculated at bias voltages corresponding to the simulated DOS in b. The simulations were carried out with a flexible CO tip (a combination of 13% of *s* and 87% of p_{xy} waves). (**B**) Spin polarized DOS of an individual pentamer with antiferromagnetic configuration. The DOS of individual charged chains do not correctly reproduce the experimental observed electronic distributions. This is caused by the delocalization effects when modeling large systems with multi-charges by DFT (detailed in Note 3). To properly simulate the electronic structures of the chain, we instead applied a model with periodic boundary condition, which captures the main features of the inner units of the pentamer as shown in Fig. 3.

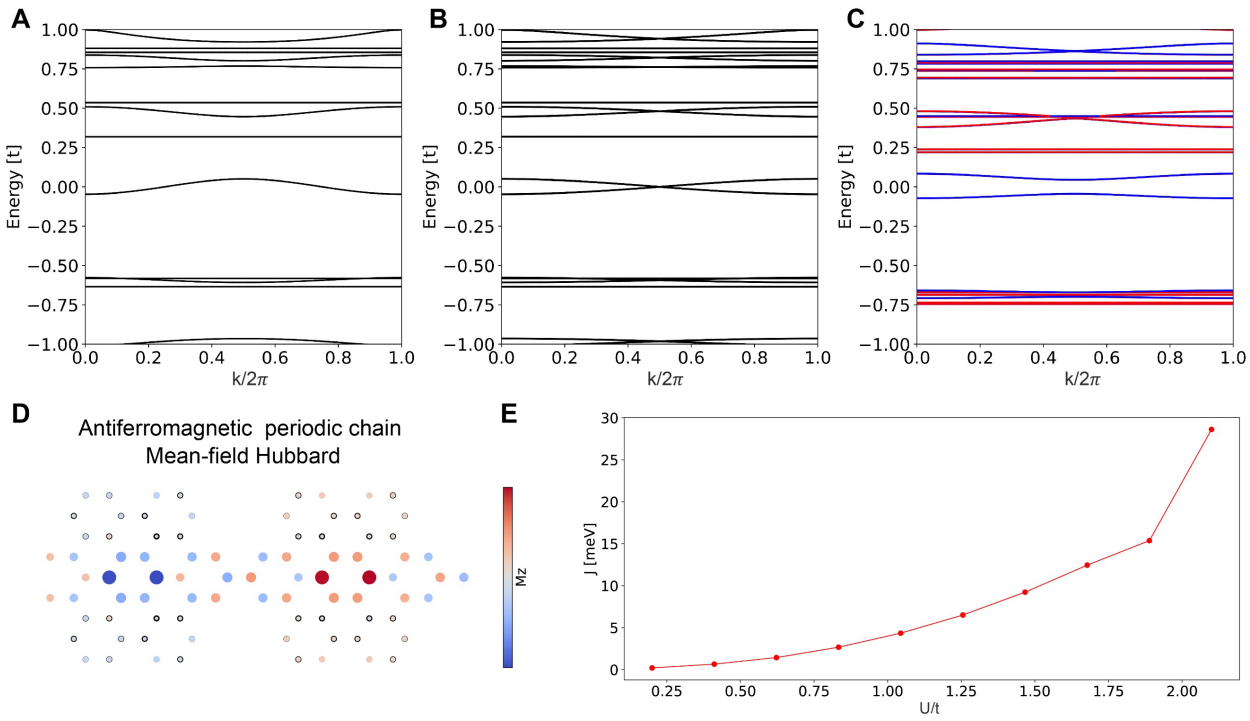

Fig. S14. Mean-field Hubbard calculations of periodic N_2HBC^+ chains. (**A**) Band structures of the periodic mono-N_2HBC^+ chain. (**B**) Periodic dimer-N_2HBC^{2+} chain and (**C**) the periodic dimer-N_2HBC^{2+} chain with an antiferromagnetic configuration. (**D**) Spin density distributions of periodic antiferromagnetic chains from mean-field Hubbard simulations (on-site Coulomb parameter was set to 2.0 eV). Red, spin up; Blue, spin down. (**E**) Exchange coupling energies J between the excitation state and antiferromagnetic ground state of the periodic chain plotted as a function of U/t. The hopping parameter t between the nearest neighbors is 2.7 eV.

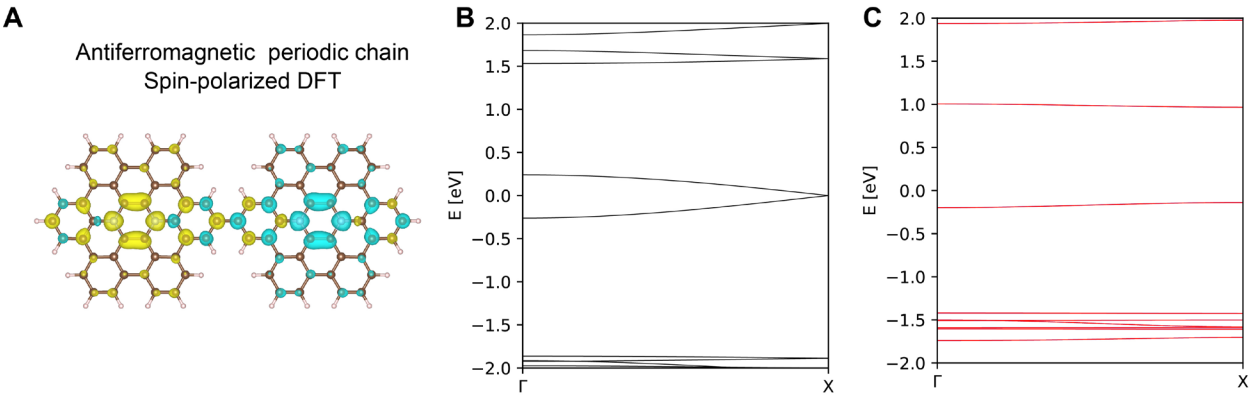

Fig. S15. Spin-polarized DFT calculations of periodic N_2HBC^+ chains. (**A**) Spin density distributions of periodic antiferromagnetic chains. Green, spin up; yellow, spin down. (**B**) Band structure of periodic dimer-N_2HBC^{2+} chains without considering spin polarization. (**C**) Band structure of spin-polarized periodic dimer-N_2HBC^{2+} chains with antiferromagnetic configuration (duplicate from Fig. 3H in the main text).

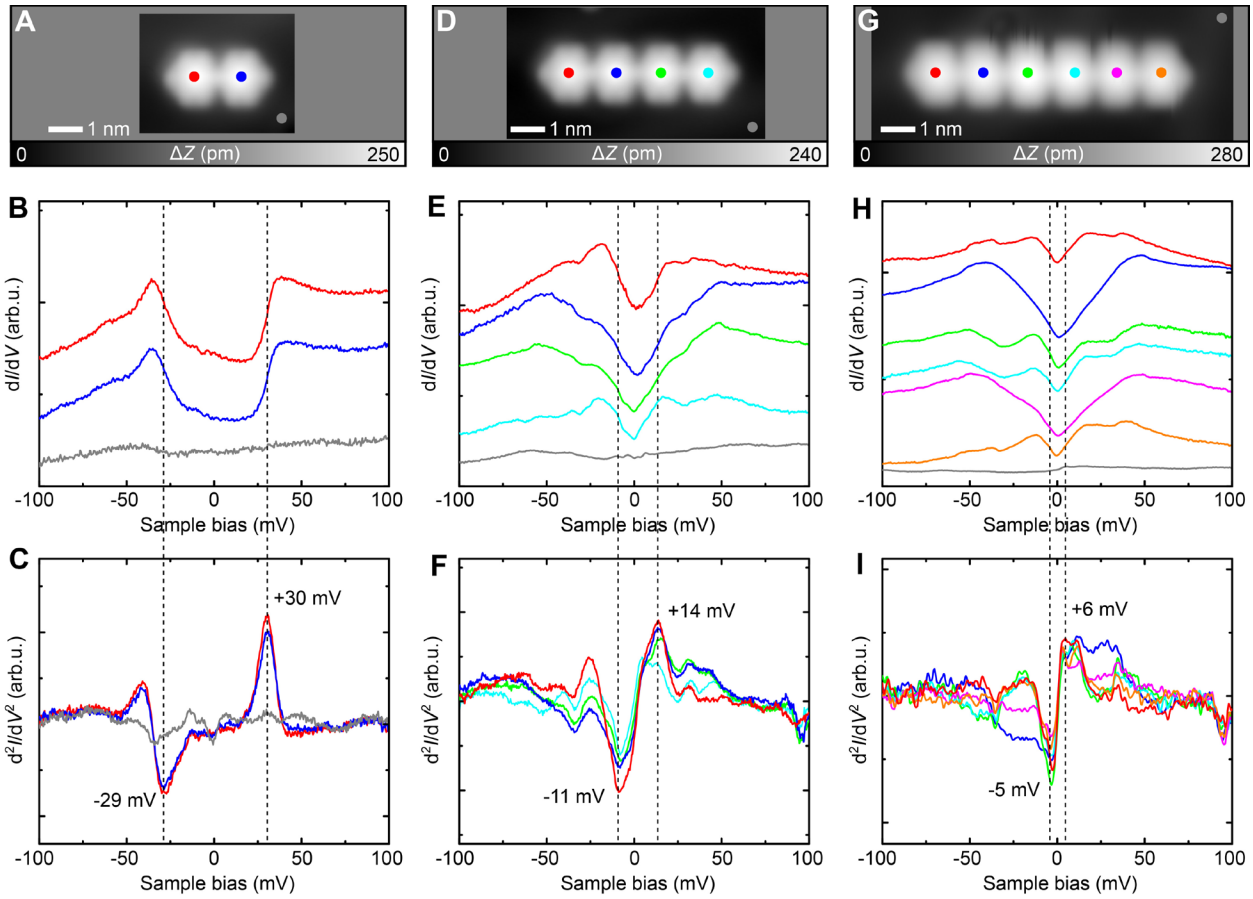

Fig. S16. Magnetic properties of dimer, tetramer and hexamer of N_2HBC. (**A**) STM topography. (**B**,**C**) dI/dV spectra (B) and d^2I/dV^2 spectra (C) recorded on the dimer and a bare Au(111) surface as indicated by colored dots in (A). (**D**) STM topography of one tetramer and (**E**,**F**) the corresponding dI/dV spectra (E) and d^2I/dV^2 spectra (F). (**G**) STM topography of one hexamer and (**H**,**I**) the corresponding dI/dV spectra (H) and d^2I/dV^2 spectra (I). The measured lowest spin excitation energies for the dimer, tetramer, and hexamer were approximately 30 mV, 14 mV, and 6 mV, respectively. Measurement parameters: V = 200 mV and I = 5 pA in (A,D). V = 200 mV and I = 10 pA in (G). V = 100 mV and I = 100-200 pA, V_{ac} = 1 mV in (B). V = 100 mV and I = 500 pA, V_{ac} = 5 mV in (C). V = 100 mV and I = 2-4 nA, V_{ac} = 1 mV in (E). V = 100 mV and I = 2 nA, V_{ac} = 5 mV in (F). V = 100 mV and I = 1-4 nA, V_{ac} = 1 mV in (H). V = 100 mV and I = 2 nA, V_{ac} = 2 mV in (I).

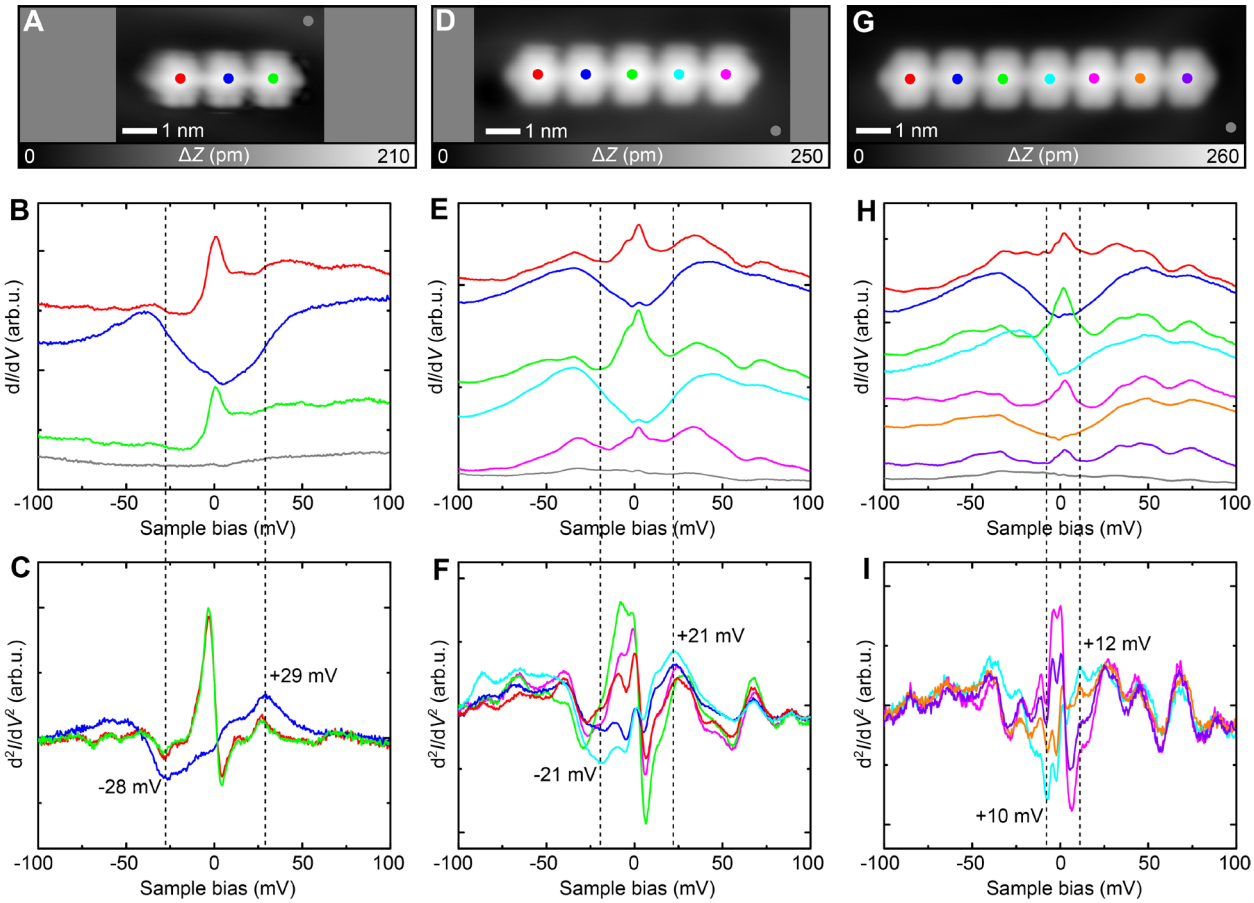

Fig. S17. Magnetic properties of trimer, pentamer and heptamer of N_2HBC. (**A**) STM topography. (**B**,**C**) dI/dV spectra (B) and d^2I/dV^2 spectra (C) recorded on the trimer and a bare Au(111) surface as indicated by colored dots in (A). (**D**) STM topography of individual tetramer and (**E**,**F**) the corresponding dI/dV spectra (E) and d^2I/dV^2 spectra (F). (**G**) STM topography of one heptamer and (**H**,**I**) the corresponding dI/dV spectra (H) and d^2I/dV^2 spectra (I). The measured lowest spin excitation energies for the trimer, pentamer, and heptamer were approximately 29 mV, 21 mV, and 12 mV, respectively. Measurement parameters: V = 200 mV and I = 3 pA in (A). V = 100 mV and I = 5 pA in (D,G). V = 100 mV and I = 200-500 pA, V_{ac} = 1 mV in (B). V = 100 mV and I = 500 pA, V_{ac} = 5 mV in (C). V = 100 mV and I = 1-4 nA, V_{ac} = 1 mV in (E). V = 100 mV and I = 1.4 nA, V_{ac} = 5 mV in (F). V = 100 mV and I = 1-4 nA, V_{ac} = 1 mV in (H). V = 100 mV and I = 1.5 nA, V_{ac} = 3 mV in (I).

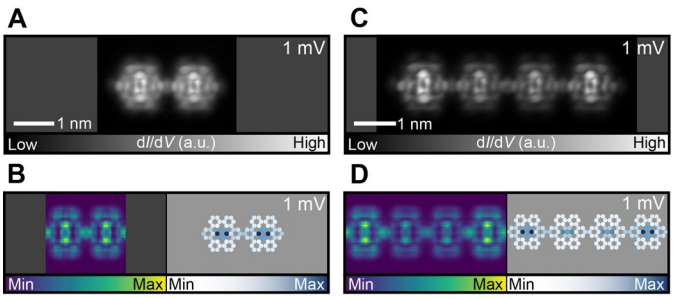

Fig. S18. Experimental and simulated d*I*/d*V* maps of dimer and tetramer of N_2HBC. (**A**,**C**) constant-height d*I*/d*V* maps of the dimer (A) and tetramer (C), taken at a bias voltage of 1 mV. (**B**,**D**) The corresponding simulated maps for dimer (B) and tetramer (D). Measurement parameters: V = 1 mV and V_{ac} = 10 mV in (A,C).

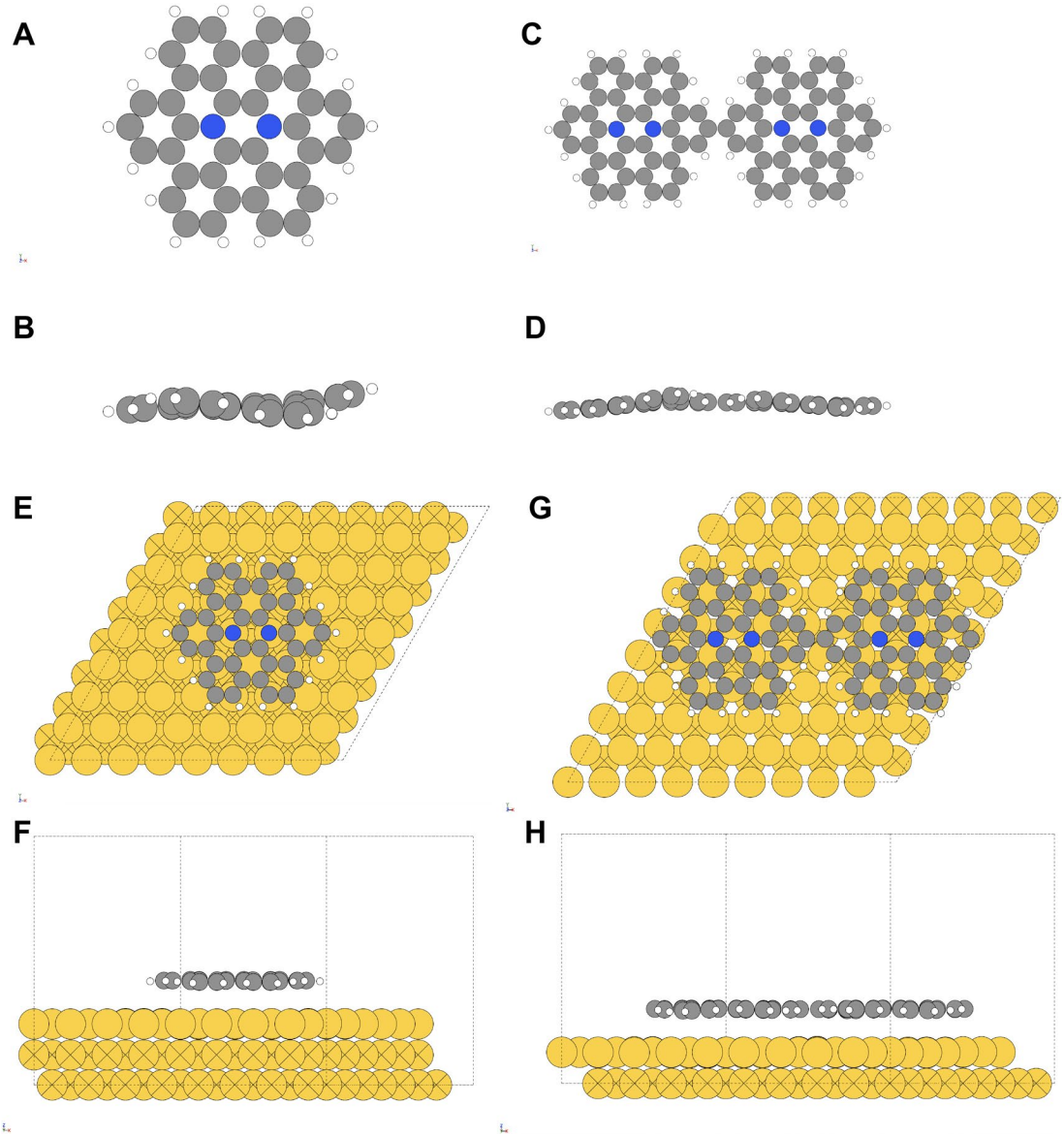

Fig. S19. DFT optimized structural models of N_2HBC^+ molecule and dimer-N_2HBC^{2+}. Gas-phase structural optimization without any constraints: (**A**,**B**) Top and side views of the N_2HBC^+ molecule and (**C**,**D**) the dimer-N_2HBC^{2+}. Structural optimization on the Au(111) surface: (**E**,**F**) Top and side views of N_2HBC^+ molecule, and (**G**,**H**) periodic N_2HBC^{2+} with dimer unit cell. In the gas phase, without any constraints, the structures are distorted while they adopt a planar structural geometry upon adsorption on the Au(111) surface.

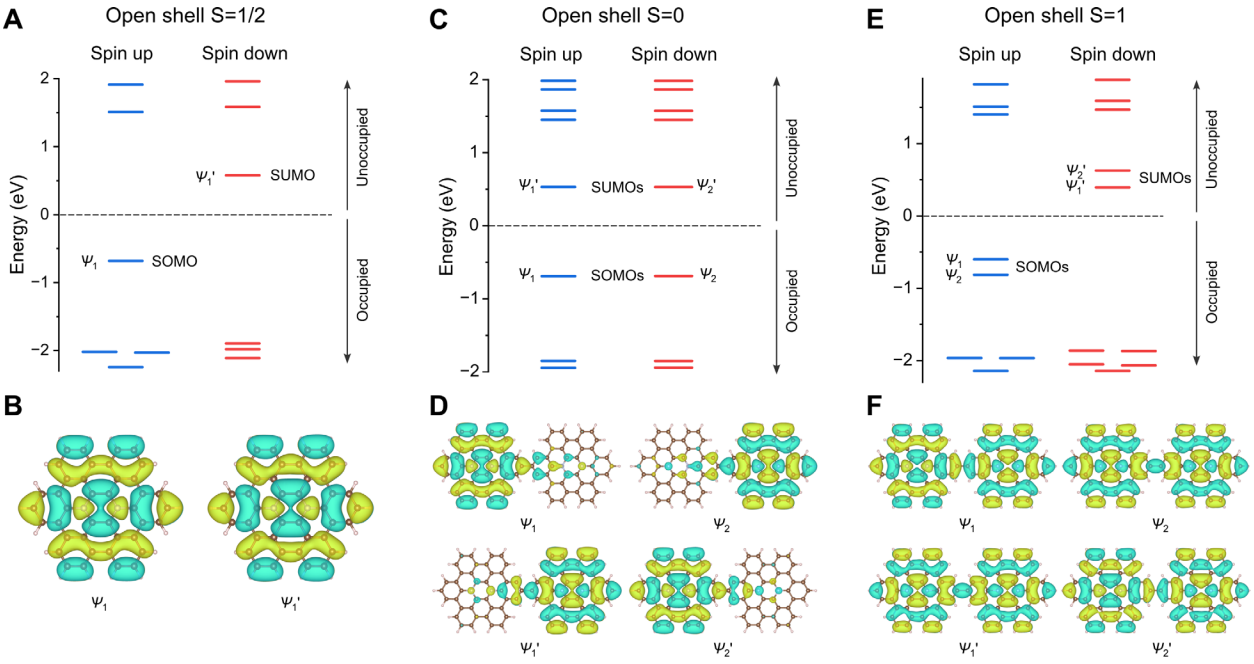

Fig. S20. Electronic structures of N_2HBC^+ molecule and dimer-N_2HBC^{2+}. (**A**) Spin-polarized DFT calculated energy spectrums of the N_2HBC^+ molecule. (**B**) Spatial distribution of the singly occupied and singly unoccupied molecular orbitals corresponding to the energy levels in (A). (**C**,**E**) Spin-polarized DFT calculated energy spectrums of the dimer-N_2HBC^{2+} for its ground singlet state (C) and excited triplet state (E), respectively. (**D**,**F**) The spatial distributions of the SOMOs (D) and LUMOs (F) corresponding to the energy levels in (C) and (E), respectively. The colors in spin distributions: green, spin up; yellow, spin down, and the isosurfaces were set to 0.02 $Å^{-3}$.

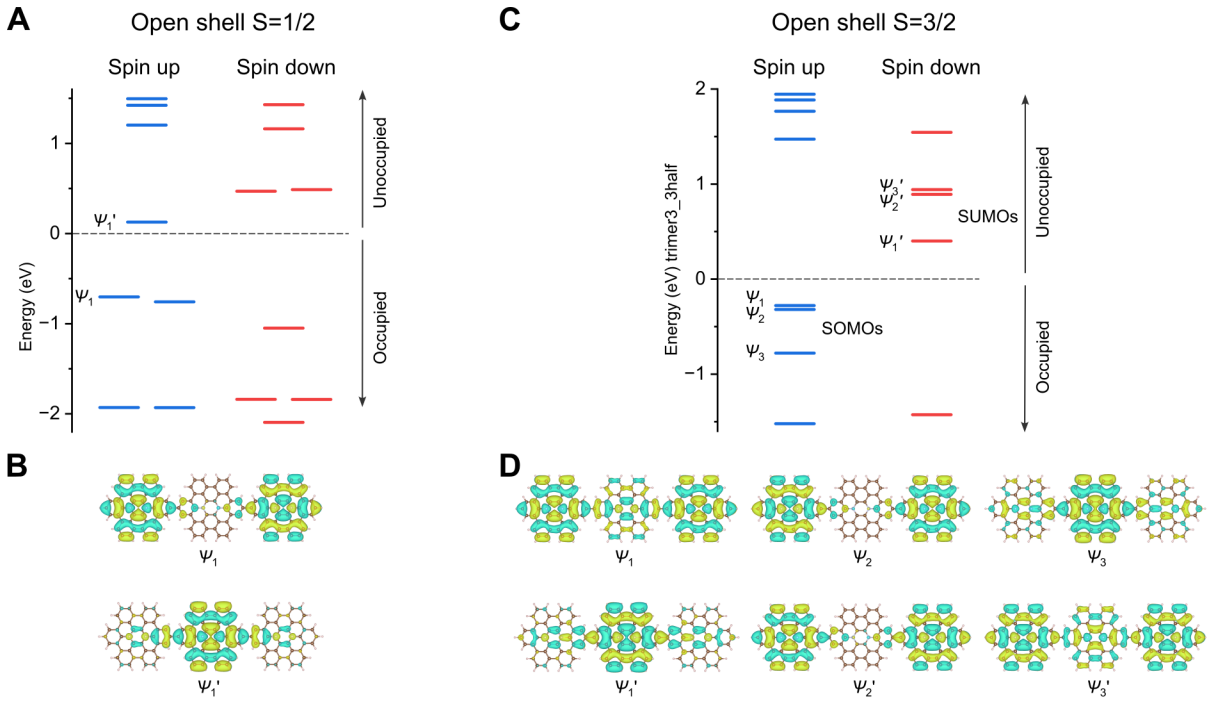

Fig. S21. Electronic structures of trimer-N_2HBC^{3+}. (**A**,**C**) Spin-polarized DFT calculated energy spectrums of the trimer-N_2HBC^{3+} for its ground doublet state (A) and excited S = 3/2 state (C), respectively. (**B**,**D**) Spatial distributions of the SOMOs (B) and LUMOs (D), among others, corresponding to the energy levels in (A) and (C), respectively. The colors in spin distributions: green, spin up; yellow, spin down, and the isosurfaces were set to 0.02 $Å^{-3}$.

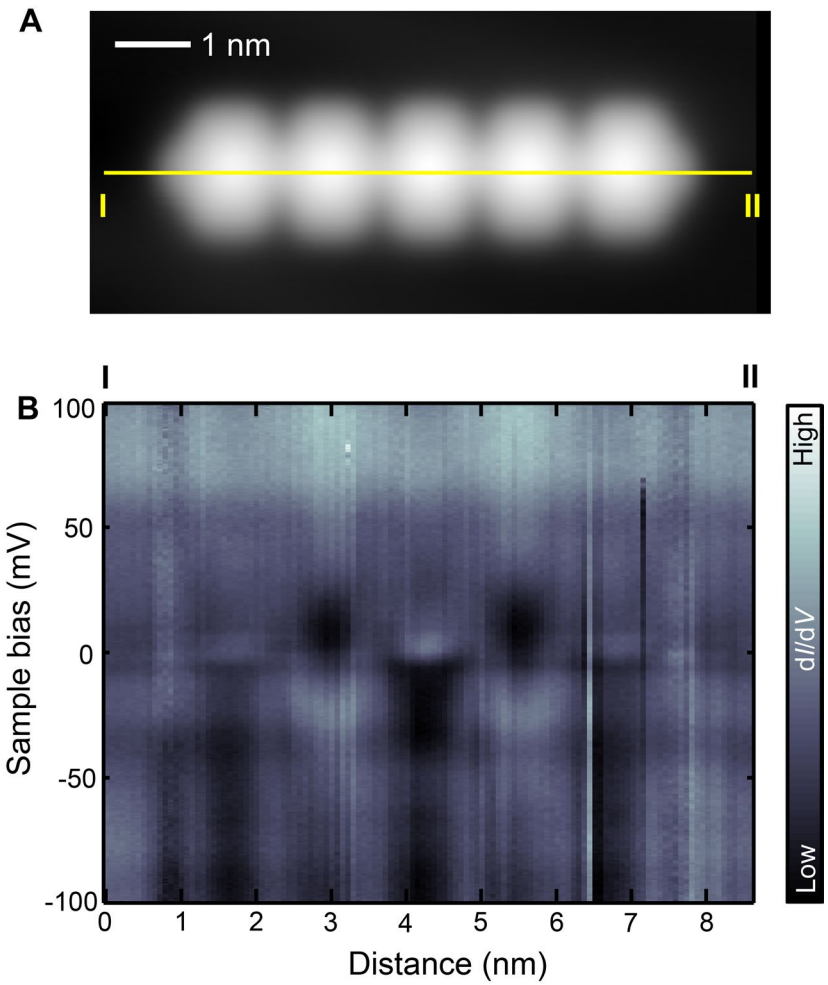

Fig. S22. **Magnetic properties of an individual pentamer of N_2HBC.** (**A**) STM topography. (**B**) Two-dimensional dI/dV maps of the pentamer, taken along I-II line. Measurement parameters: V = 200 mV and I = 10 pA in (A). V = 100 mV, I = 300 pA, V_{ac} = 1 mV and f = 510 Hz in (B).

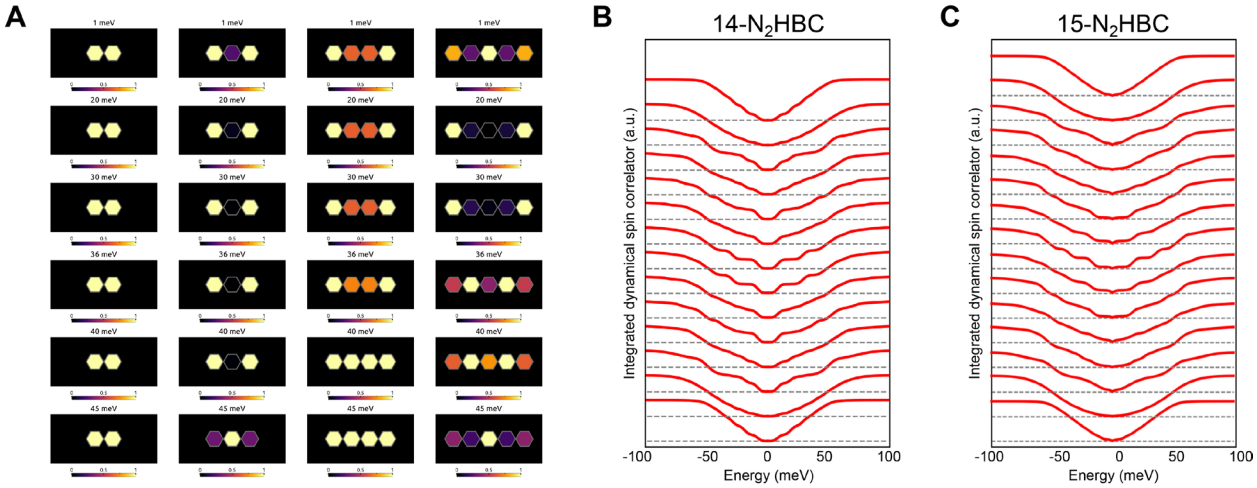

Fig. S23. DSC maps at different energies and the Heisenberg model applied to longer chains. (**A**) Simulated dI/dV normalized maps from dimer to pentamer obtained using our low energy model at several different energies. (**B**,**C**) Integrated dynamical spin correlator corresponding to 14- (B) and 15-N_2HBC chains (C), showing that the Kondo peaks are quenched regardless of the parity of longer chains.

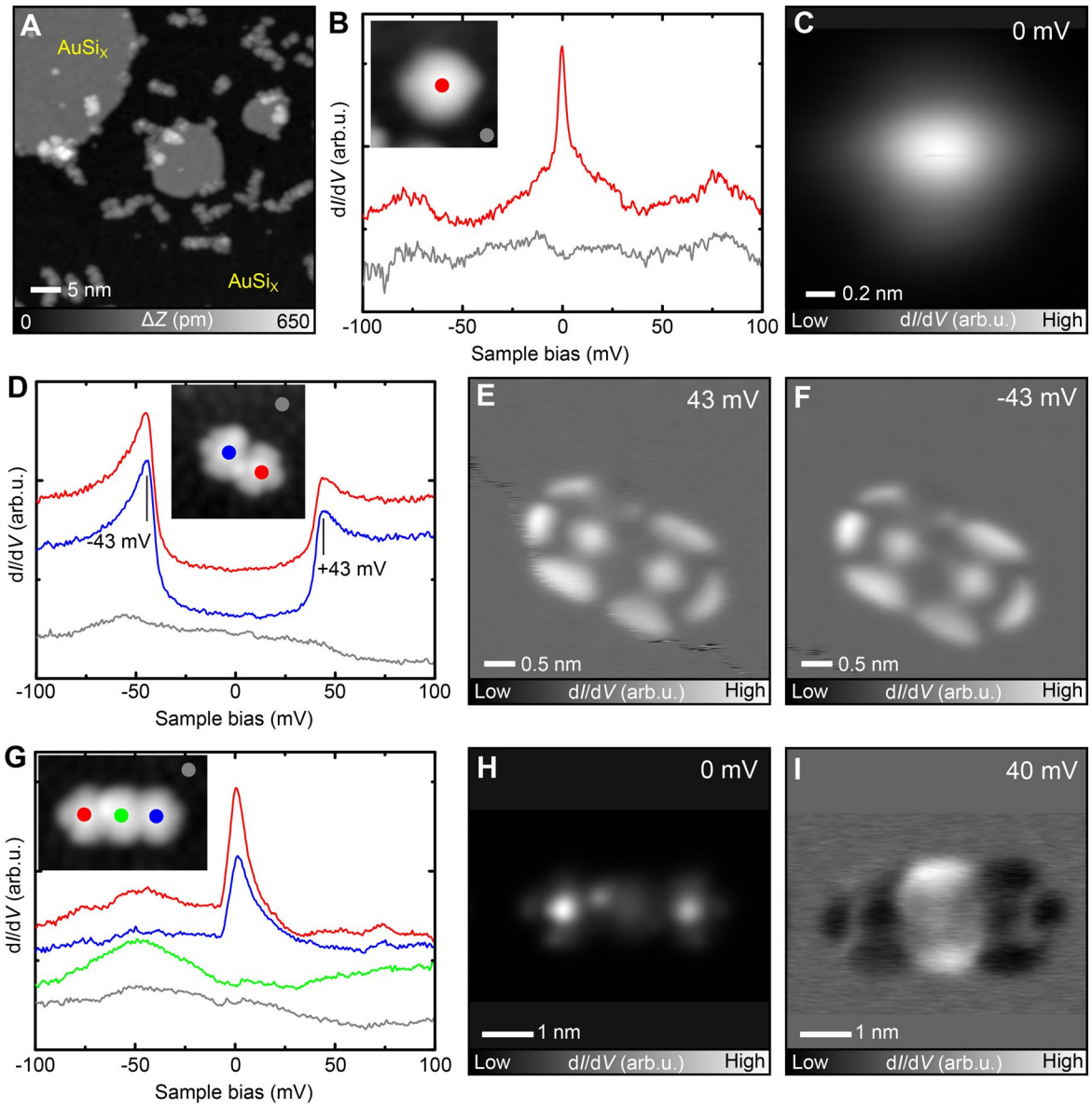

Fig. S24. Magnetic properties of monomer, dimer and trimer of N_2HBC on a AuSi$_X$ layer formed on Au(111). (**A**) STM topography after depositing Si atoms on the substrate kept at 150 °C. (**B**) dI/dV curves measured at different sites as indicated by colored dots. Inset shows one monomer on the AuSi$_X$/Au(111) surface. (**C**) Constant height dI/dV map measured above the monomer at sample bias voltage of 0 V. (**D**) dI/dV curves measured at different sites as indicated by colored dots. Inset shows one dimer on the AuSi$_X$/Au(111) surface. (**E**,**F**) Constant current dI/dV maps measured above the dimer at sample bias voltages of 43 mV, -43 mV, respectively. (**G**) dI/dV curves measured at different sites as indicated by colored dots. Inset shows one trimer on the AuSi$_X$/Au(111) surface. (**H**) Constant height dI/dV map measured above the trimer in (G) at sample bias voltage of 0 V. (**I**) Constant current dI/dV map measured above the trimer at sample bias voltages of 40 mV. Measurement parameters: V = 300 mV and I = 1.8 pA in (A).

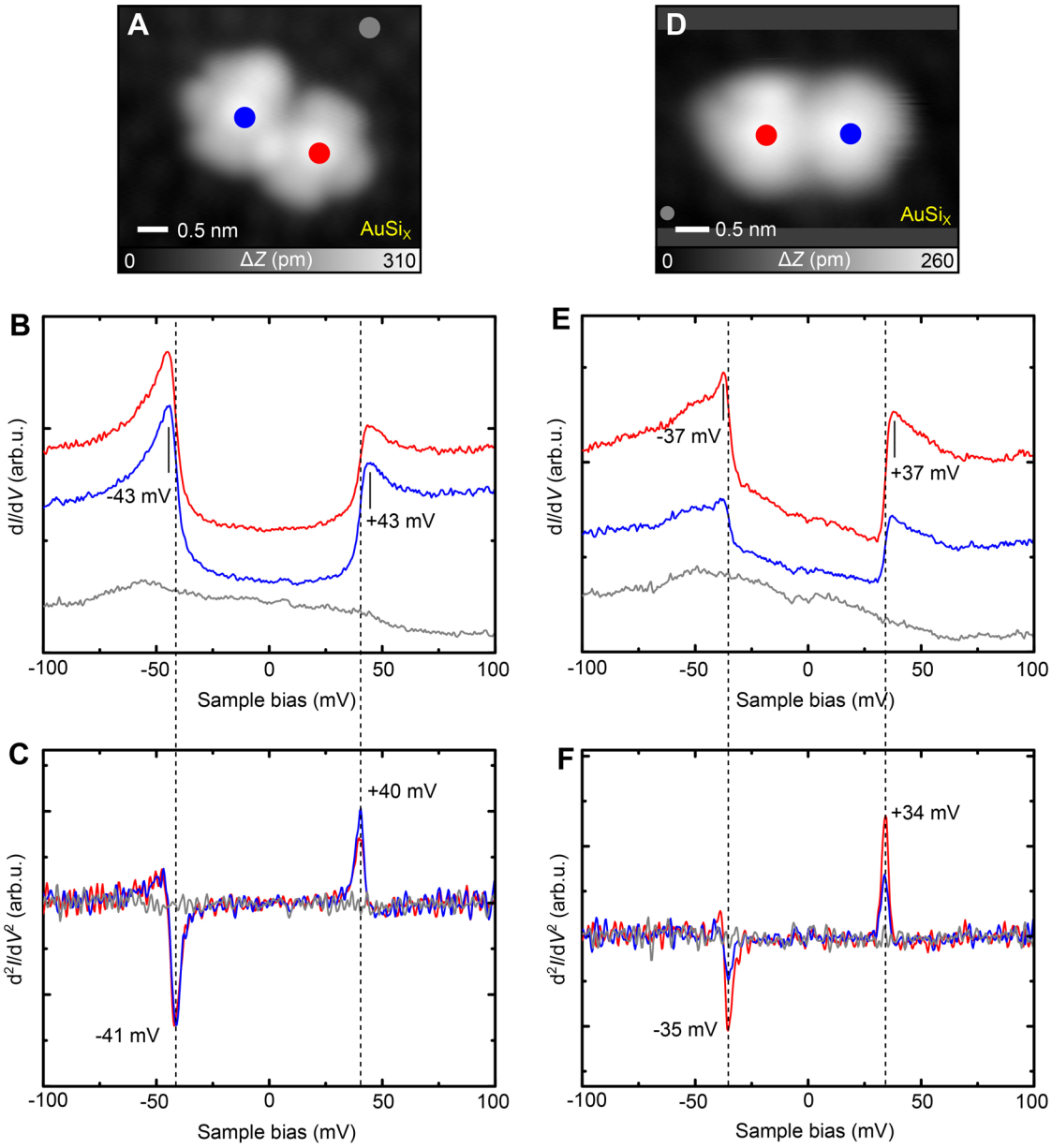

Fig. S25. Magnetic properties of two dimers on a AuSix layer formed on Au(111). (**A**) STM topography of one dimer on the AuSiX/Au(111) surface. (**B**) dI/dV spectra recorded on the dimer and AuSiX sunstrate, as indicated by colored dots in (A). dI/dV curves in (B) is identical to those in fig. S24D. (**C**) d^2I/dV^2 curves derived from the differentiation of the curves in (A). (**D**) STM topography of another dimer on the AuSiX/Au(111) surface. (**E**) dI/dV spectra recorded on the dimer and AuSiX substrate. (**F**) d^2I/dV^2 curves derived from the differentiation of the curves in (E). Measurement parameters: V = 200 mV and I = 5 pA in (A). V = 100 mV and I = 2 pA in (D). V = 100 mV and I = 200 pA, V_{ac} = 1 mV in (B,E).

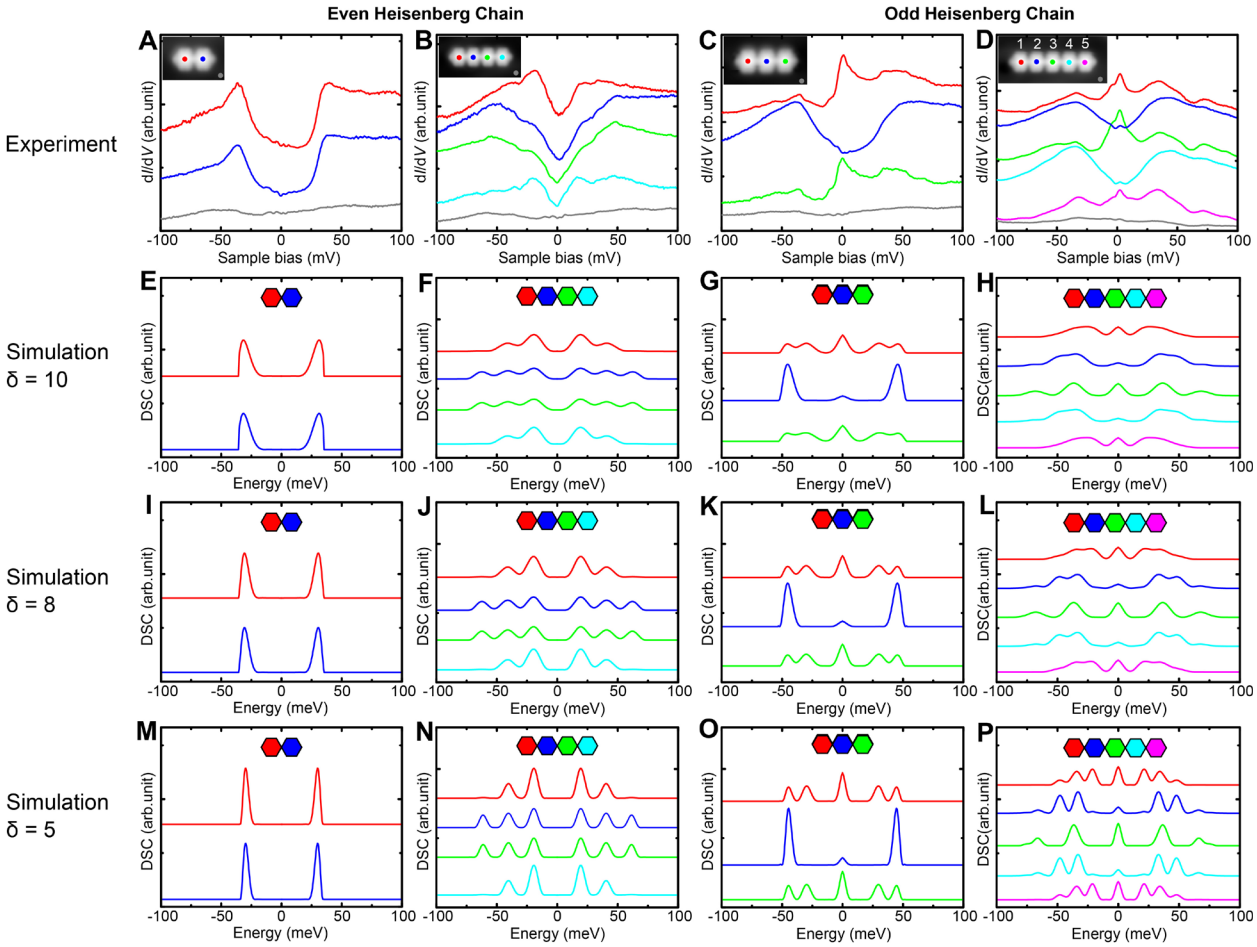

Fig. S26. Simulations of spin excitations with different broadening effects (δ = 10, 8, 5). (**A-D**) Experimental d*I*/d*V* spectra taken at the center of each unit of even- and odd-numbered chains. (**E-P**) Theoretical calculations of spin excitations for the chains with different broadening effects (δ = 10, 8, 5) applied to simulate the experimental condition. The simulated spectra show good resolution for higher energy excitations when a small broadening factor (δ = 5) is applied.

Table S1. Various types of calculated energies. Vacuum energy (E_{vac}), Fermi level (E_F) and work functions ($\phi_{wf} = E_{vac} - E_F$) calculated using PBE for the N_2HBC molecule, dimer-N_2HBC and trimer-N_2HBC. The reference value used for Au(111) was also calculated with PBE.

	N_2HBC molecule		dimer-N_2HBC		trimer-N_2HBC		Au(111)
	neutral	1+ charge	neutral	2+ charge	neutral	3+ charge	-
E_{vac}	-0.073	0.104	-0.135	0.170	-0.146	0.205	-
E_F	-3.245	-5.539	-3.336	-5.511	-3.246	-5.626	-
ϕ_{wf}	**3.17**	**5.64**	**3.20**	**5.68**	**3.10**	**5.83**	**5.19** (*55*)

REFERENCES AND NOTES

1. J. Fernández-Rossier, J. J. Palacios, Magnetism in graphene nanoislands. *Phys. Rev. Lett.* **99**, 177204 (2007).

2. A. R. Rocha, V. M. García-suárez, S. W. Bailey, C. J. Lambert, J. Ferrer, S. Sanvitoet, Towards molecular spintronics. *Nat. Mater.* **4**, 335–339 (2005).

3. O. V. Yazyev, Emergence of magnetism in graphene materials and nanostructures. *Rep. Prog. Phys.* **73**, 056501 (2010).

4. D. Pesin, A. H. MacDonald, Spintronics and pseudospintronics in graphene and topological insulators. *Nat. Mater.* **11**, 409–416 (2012).

5. H. Min, J. E. Hill, N. A. Sinitsyn, B. R. Sahu, L. Kleinman, A. H. MacDonald, Intrinsic and Rashba spin-orbit interactions in graphene sheets. *Phys. Rev. B.* **74**, 165310 (2007).

6. O. V. Yazyev, M. I. Katsnelson, Magnetic correlations at graphene edges: Basis for novel spintronics devices. *Phys. Rev. Lett.* **100**, 047209 (2008).

7. N. Tombros, C. Jozsa, M. Popinciuc, H. T. Jonkman, B. J. van Wees, Electronic spin transport and spin precession in single graphene layers at room temperature. *Nature* **448**, 571–574 (2007).

8. O. V. Yazyev, Hyperfine interactions in graphene and related carbon nanostructures. *Nano Lett.* **8**, 1011–1015 (2008).

9. F. Lombardi, A. Lodi, J. Ma, J. Liu, M. Slota, A. Narita, W. Myers, K. Müllen, X. Feng, L. Bogani, Quantum units from the topological engineering of molecular graphenoids. *Science* **366**, 1107–1110 (2019).

10. L. Grill, S. Hecht, Covalent on-surface polymerization. *Nat. Chem.* **12**, 115–130 (2020).

11. L. Grill, M. Dyer, L. Lafferentz, M. Persson, M. V. Peters, S. Hecht, Nano-architectures by covalent assembly of molecular building blocks. *Nat. Nanotechnol.* **2**, 687–691 (2007).

12. D. G. de Oteyza, T. Frederiksen, Carbon-based nanostructures as a versatile platform for tunable π-magnetism. *J. Phys. Condens. Matter* **34**, 443001 (2022).

13. S. Mishra, D. Beyer, K. Eimre, S. Kezilebieke, R. Berger, O. Gröning, C. A. Pignedoli, K. Müllen, P. Liljeroth, P. Ruffieux, X. Feng, R. Fasel, Topological frustration induces unconventional magnetism in a nanographene. *Nat. Nanotechnol.* **15**, 22–28 (2020).

14. J. Li, S. Sanz, M. Corso, D. J. Choi, D. Peña, T. Frederiksen, J. I. Pascual, Single spin localization and manipulation in graphene open-shell nanostructures. *Nat. Commun.* **10**, 200 (2009).

15. S. Mishra, D. Beyer, K. Eimre, J. Liu, R. Berger, O. Gröning, C. A. Pignedoli, K. Müllen, R. Fasel, X. Feng, P. Ruffieux, Synthesis and characterization of π-extended triangulene. *J. Am. Chem. Soc.* **141**, 10621–10625 (2019).

16. J. Su, M. Telychko, P. Hu, G. Macam, P. Mutombo, H. Zhang, Y. Bao, F. Cheng, Z.-Q. Huang, Z. Qiu, S. J. R. Tan, H. Lin, P. Jelínek, F.-C. Chuang, J. Wu, J. Lu, Atomically precise bottom-up synthesis of π-extended [5]triangulene. *Sci. Adv.* **5**, eaav7717 (2019).

17. J. Li, S. Sanz, J. Castro-Esteban, M. Vilas-Varela, N. Friedrich, T. Frederiksen, D. Peña, J. I. Pascual, Uncovering the triplet ground state of triangular graphene nanoflakes engineered with atomic precision on a metal surface. *Phys. Rev. Lett.* **124**, 177201 (2020).

18. Y. Zheng, C. Li, C. Xu, D. Beyer, X. Yue, Y. Zhao, G. Wang, D. Guan, Y. Li, H. Zheng, C. Liu, J. Liu, X. Wang, W. Luo, X. Feng, S. Wang, J. Jia, Designer spin order in diradical nanographenes. *Nat. Commun.* **11**, 6076 (2020).

19. Q. Sun, X. Yao, O. Gröning, K. Eimre, C. A. Pignedoli, K. Müllen, A. Narita, R. Fasel, P. Ruffieux, Coupled spin states in armchair graphene nanoribbons with asymmetric zigzag edge extensions. *Nano Lett.* **20**, 6429–6436 (2020).

20. S. Mishra, X. Yao, Q. Chen, K. Eimre, O. Gröning, R. Ortiz, M. Di Giovannantonio, J. C. Sancho-García, J. Fernández-Rossier, C. A. Pignedoli, K. Müllen, P. Ruffieux, A. Narita, R.

Fasel, Large magnetic exchange coupling in rhombus-shaped nanographenes with zigzag periphery. *Nat. Chem.* **13**, 581–586 (2021).

21. K. Sun, O. J. Silveira, S. Saito, K. Sagisaka, S. Yamaguchi, A. S. Foster, S. Kawai, Manipulation of spin polarization in boron-substituted graphene nanoribbons. *ACS Nano* **16**, 11244–11250 (2022).

22. X. Xu, K. Sun, A. Ishikawa, A. Narita, S. Kawai, Magnetism in nonplanar zigzag edge termini of graphene nanoribbons. *Angew. Chem. Int. Ed.* **62**, e202302534 (2023).

23. R. D. McCurdy, A. Delgado, J. Jiang, J. Zhu, E. C. H. Wen, R. E. Blackwell, G. C. Veber, S. Wang, S. G. Louie, F. R. Fischer, Engineering robust metallic zero-mode states in olympicene graphene nanoribbons. *J. Am. Chem. Soc.* **145**, 15162–15170 (2023).

24. C. Zhao, G. Catarina, L. Zhang, J. C. G. Henriques, L. Yang, J. Ma, X. Feng, O. Gröning, P. Ruffieux, J. Fernández-Rossier, R. Fasel, Tunable topological phases in nanographene-based spin-½ alternating-exchange Heisenberg chains. *Nat. Nanotechnol.* **19**, 1789–1795 (2024).

25. J. Hieulle, S. Castro, N. Friedrich, A. Vegliante, F. R. Lara, S. Sanz, D. Rey, M. Corso, T. Frederiksen, J. I. Pascual, D. Peña, On-surface synthesis and collective spin excitations of a triangulene-based nanostar. *Angew. Chem. Int. Ed.* **60**, 25224–25229 (2021).

26. S. Mishra, G. Catarina, F. Wu, R. Ortiz, D. Jacob, K. Eimre, J. Ma, C. A. Pignedoli, X. Feng, P. Ruffieux, J. Fernández-Rossier, R. Fasel, Observation of fractional edge excitations in nanographene spin chains. *Nature* **598**, 287–292 (2021).

27. Y. Zhao, K. Jiang, C. Li, Y. Liu, G. Zhu, M. Pizzochero, E. Kaxiras, D. Guan, Y. Li, H. Zheng, C. Liu, J. Jia, M. Qin, X. Zhuang, S. Wang, Quantum nanomagnets in on-surface metal-free porphyrin chains. *Nat. Chem.* **15**, 53–60 (2023).

28. E. C. Ho Wen, P. H. Jacobse, J. Jiang, Z. Wang, R. D. McCurdy, S. G. Louie, M. F. Crommie, R. Fischer, Magnetic interactions in substitutional core-doped graphene nanoribbons. *J. Am. Chem. Soc.* **144**, 13696–13703 (2022).

29. E. C. H. Wen, P. H. Jacobse, J. Jiang, Z. Wang, S. G. Louie, M. F. Crommie, F. R. Fischer, Fermi-level engineering of nitrogen core-doped armchair graphene nanoribbons. *J. Am. Chem. Soc.* **145**, 19338–19346 (2023).

30. H. Z. Bethe, Zur Theorie der Metalle. *Zeitschrift für Physik* **71**, 205–226 (1931).

31. S. Murmann, F. Deuretzbacher, G. Zürn, J. Bjerlin, S. M. Reimann, L. Santos, T. Lompe, S. Jochim, Antiferromagnetic Heisenberg spin chain of few cold atoms in a one-dimensional trap. *Phys. Rev. Lett.* **115**, 215301 (2015).

32. X.-Y. Wang, M. Richter, Y. He, J. Björk, A. Riss, R. Rajesh, M. Garnica, F. Hennersdorf, J. J. Weigand, A. Narita, R. Berger, X. Feng, W. Auwärter, J. V. Barth, C.-A. Palma, K. Müllen, Exploration of pyrazine-embedded antiaromatic polycyclic hydrocarbons generated by solution and on-surface azomethine ylide homocoupling. *Nat. Commun.* **8**, 1948 (2017).

33. R. Berger, A. Giannakopoulos, P. Ravat, M. Wagner, D. Beljonne, X. Feng, K. Müllen, Synthesis of nitrogen-doped zigzag-edge peripheries: Dibenzo-9a-azaphenalene as repeating unit. *Angew. Chem. Int. Ed.* **53**, 10520–10524 (2014).

34. R. Temirov, S. Soubatch, O. Neucheva, A. C. Lassise, F. S. Tautz, A novel method achieving ultra-high geometrical resolution in scanning tunnelling microscopy. *New J. Phys.* **10**, 053012 (2008).

35. L. Gross, F. Mohn, N. Moll, P. Liljeroth, G. Meyer, The chemical structure of a molecule resolved by atomic force microscopy. *Science* **325**, 1110–1114 (2009).

36. X. Chen, Y.-S. Fu, S.-H. Ji, T. Zhang, P. Cheng, X.-C. Ma, X.-L. Zou, W.-H. Duan, J.-F. Jia, Q.-K. Xue, Probing superexchange interaction in molecular magnets by spin-flip spectroscopy and microscopy. *Phys. Rev. Lett.* **101**, 197208 (2008).

37. D. Jacob, J. Fernández-Rossier, Theory of intermolecular exchange in coupled spin- 1/2 nanographenes. *J. Phys. Rev. B* **106**, 205405 (2022).

38. Y. Saleem, T. Steenbock, E. R. J. Alhadi, W. Pasek, G. Bester, P. Potasz, Superexchange mechanism in coupled triangulenes forming spin-1 chains. *Nano Lett.* **24**, 7417–7423 (2024).

39. M. Fishman, E. Stoudenmire, ITensor Team. ITensor Library. GitHub, https://github.com/ITensor/ITensor.

40. M. Fishman, S. R. White, E. M. Stoudenmire, The ITensor software library for tensor network calculations. *SciPost Phys. Codebases* **4**, 10.21468/SciPostPhysCodeb.4 (2022).

41. DMRGpy Library, http://github.com/joselado/dmrgpy.

42. J. Fernández-Rossier, Theory of single-spin inelastic tunneling spectroscopy. *Phys. Rev. Lett.* **102**, 256802 (2009).

43. O. Deniz, C. Sánchez-Sánchez, T. Dumslaff, X. Feng, A. Narita, K. Müllen, N. Kharche, V. Meunier, R. Fasel, P. Ruffieux, Revealing the electronic structure of silicon intercalated armchair graphene nanoribbons by scanning tunneling spectroscopy. *Nano Lett.* **17**, 2197–2203 (2017).

44. K. Sun, S. Kawai, Strength of electronic decoupling of fullerene on an $AuSi_X$ layer formed on Au(111). *Phys. Chem. Chem. Phys.* **23**, 5455–5459 (2021).

45. V. Blum, R. Gehrke, F. Hanke, P. Havu, V. Havu, X. Ren, K. Reuter, M. Scheffler, Ab initio molecular simulations with numeric atom-centered orbitals. *Comput. Phys. Commun.* **180**, 2175–2196 (2009).

46. J. P. Perdew, K. Burke, M. Ernzerhof, Generalized gradient approximation made simple. *Phys. Rev. Lett.* **77**, 3865–3868 (1996).

47. A. D. Becke, Density-functional thermochemistry. III. The role of exact exchange. *J. Chem. Phys.* **98**, 5648–5652 (1993).

48. J. L. Lado, Pyqula, GitHub, https://github.com/joselado/pyqula.

49. P. Hapala, G. Kichin, C. Wagner, F. S. Tautz, R. Temirov, P. Jelínek, Mechanism of high-resolution STM/AFM imaging with functionalized tips. *Phys. Rev. B* **90**, 085421 (2014).

50. B. de la Torre, M. Švec, G. Foti, O. Krejčí, P. Hapala, A. Garcia-Lekue, T. Frederiksen, R. Zbořil, A. Arnau, H. Vázquez, P. Jelínek, Submolecular resolution by variation of the inelastic electron tunneling spectroscopy amplitude and its relation to the AFM/STM signal. *Phys. Rev. Lett.* **119**, 166001 (2017).

51. L. Gross, N. Moll, F. Mohn, A. Curioni, G. Meyer, F. Hanke, M. Persson, High-resolution molecular orbital imaging using a *p*-wave STM tip. *Phys. Rev. Lett.* **107**, 086101 (2011).

52. O. Krejčí, P. Hapala, M. Ondráček, P. Jelínek, Principles and simulations of high-resolution STM imaging with a flexible tip apex. *Phys. Rev. B* **95**, 045407 (2017).

53. W. C. Still, M. Kahn, A. Mitra, Rapid chromatographic technique for preparative separations with moderate resolution. *J. Org. Chem.* **43**, 2923–2925 (1978).

54. B. Yang, J. Yang, J. Zhang, Synthesis of axially chiral anilides enabled by a palladium/ming-phos-catalyzed desymmetric Sonogashira reaction. *Chin. J. Chem.* **40**, 317–322 (2021).

55. S.-U. Yoo, N. Siemer, M. Todorova, D. Marx, J. Neugebauer, Deciphering charge transfer and electronic polarization effects at gold nanocatalysts on reduced titania support. *J. Phys. Chem. C* **123**, 5495–5506 (2019).